Brain implantation of soft bioelectronics via embryonic development

https://doi.org/10.1038/s41586-025-09106-8

Received: 27 September 2022

Accepted: 6 May 2025

Hao Sheng[1,11], Ren Liu[1,11], Qiang Li[1,11], Zuwan Lin[2,11], Yichun He[1], Thomas S. Blum[1], Hao Zhao[1], Xin Tang[1], Wenbo Wang[1], Lishuai Jin[3], Zheliang Wang[4], Emma Hsiao[1], Paul Le Floch[1,5], Hao Shen[1], Ariel J. Lee[1,6], Rachael Alice Jonas-Closs[7], James Briggs[8], Siyi Liu[4], Daniel Solomon[1], Xiao Wang[8,9], Jessica L. Whited[10], Nanshu Lu[4] & Jia Liu[1]✉

Developing bioelectronics capable of stably tracking brain-wide, single-cell, millisecond-resolved neural activity in the developing brain is critical for advancing neuroscience and understanding neurodevelopmental disorders. During development, the three-dimensional structure of the vertebrate brain arises from a two-dimensional neural plate[1,2]. These large morphological changes have previously posed a challenge for implantable bioelectronics to reliably track neural activity throughout brain development[3–9]. Here we introduce a tissue-level-soft, submicrometre-thick mesh microelectrode array that integrates into the embryonic neural plate by leveraging the tissue's natural two-dimensional-to-three-dimensional reconfiguration. As organogenesis progresses, the mesh deforms, stretches and distributes throughout the brain, seamlessly integrating with neural tissue. Immunostaining, gene expression analysis and behavioural testing confirm no adverse effects on brain development or function. This embedded electrode array enables long-term, stable mapping of how single-neuron activity and population dynamics emerge and evolve during brain development. In axolotl models, it not only records neural electrical activity during regeneration but also modulates the process through electrical stimulation.

Tracking neural activities throughout brain development is critical to understanding how neurons self-assemble into an organ capable of learning, behaviour and cognition[1]. However, achieving brain-wide, single-cell, millisecond-resolution recording throughout brain development remains a challenge[3–6]. Functional magnetic resonance imaging enables non-invasive, brain-wide activity mapping[7], but lacks high spatiotemporal resolution. Microscopic imaging using genetically encoded calcium or voltage indicators provides cell-specific imaging but is limited to transparent species such as larval zebrafish[8]. In non-transparent animals, tissue scattering and volumetric scanning, however, limit fast optical access to neurons throughout three-dimensional (3D) brain structures.

Implanted microelectrodes offer a potential solution, enabling single-unit recordings with millisecond precision in 3D tissue. Multielectrode arrays can simultaneously track activity from large neural populations without compromising spatial or temporal resolution[10–13]. The developing brain, however, presents additional challenges. Vertebrate brains are complex 3D structures that originate from a two-dimensional (2D) single-cell layer in the embryo. During development, cell division, proliferation and folding events result in rapid volume expansion and large changes in tissue morphology[14–16]. Conventional microelectronics cannot interrogate such dynamically changing environments with accuracy, compatibility and longevity owing to fundamental mechanical mismatches between electronic and biological materials.

Recent advances in flexible electronics[17–20] have led to 'tissue-like' mesh microelectronics—submicrometre-thick mesh structures with tissue-level flexibility. These devices mimic the physicochemical properties of the extracellular matrix, enabling seamless integration into in vitro and in vivo neural tissues. They form gliosis-free bioelectronic interfaces supporting long-term, stable, multichannel electrical recordings in 3D brain tissues at single-spike resolution over months[21]. However, in mature brains, neurons are innervated at the nanometre scale. Regardless of how small and soft bioelectronics are designed, implantation into mature brains inevitably causes acute damage. We previously demonstrated that stretchable electronics could be integrated into developing tissue in vitro via normal developmental processes[22,23]. The endogenous forces from tissue growth unfold and distribute the bioelectronics throughout the 3D structure, allowing stable long-term interfacing.

Here we report bioelectronic devices and implantation methods for seamless integration into developing vertebrate brains throughout embryogenesis. Specifically, our submicrometre-thick, tissue-level-soft mesh electronics contain a stretchable electrode array that can be implanted into the embryonic neural plate. As the neural plate undergoes 2D-to-3D reorganization during organogenesis[2], endogenous

---

[1]John A. Paulson School of Engineering and Applied Sciences, Harvard University, Boston, MA, USA. [2]Department of Chemistry and Chemical Biology, Harvard University, Cambridge, MA, USA. [3]Department of Materials Science and Engineering, University of Pennsylvania, Philadelphia, PA, USA. [4]Department of Aerospace Engineering and Engineering Mechanics, The University of Texas at Austin, Austin, TX, USA. [5]Axoft Inc., Cambridge, MA, USA. [6]Electrical Engineering and Computer Science, MIT, Cambridge, MA, USA. [7]Department of Systems Biology, Harvard Medical School, Boston, MA, USA. [8]Broad Institute of MIT and Harvard, Cambridge, MA, USA. [9]Department of Chemistry, MIT, Cambridge, MA, USA. [10]Department of Stem Cell and Regenerative Biology, Harvard University, Cambridge, MA, USA. [11]These authors contributed equally: Hao Sheng, Ren Liu, Qiang Li, Zuwan Lin. ✉e-mail: jia_liu@seas.harvard.edu

forces naturally distribute and integrate the mesh across the 3D volume of the neural tube and brain, creating a 'cyborg' embryo. We refer to embryos and tadpoles with embedded electronics as 'cyborg embryos' and 'cyborg tadpoles', and controls are animals without embedded devices. Our study confirms that the embedded microelectronics do not impact embryo development or behaviour. The device enables continuous, brain-wide neural recording at millisecond resolution, capturing the emergence, synchronization and propagation of neural dynamics throughout embryonic brain development.

Soft bioelectronics for embryonic brain

During vertebrate development, the neural plate, a 2D, single-cell, ectoderm-derived layer on the embryo's surface, folds to form the neural tube and, with continued expansion and folding, morphs into the 3D brain and other parts of the nervous system[2]. We predicted that this 2D-to-3D transformation could naturally integrate soft, stretchable bioelectronics into the developing brain with minimal impact. To test this, we used *Xenopus laevis* (frog) embryos (Fig. 1a), a widely studied model in developmental biology that allows direct access to the neural plate in aqueous conditions[1]. Mesh electronics containing a stretchable electrode array are non-invasively implanted and driven by the 2D-to-3D reconfiguration of the neural tissue during neurulation (Fig. 1b). As the neural tube forms into a 3D structure, the stretchable electrode array fully integrates with neural networks throughout the brain (Fig. 1c), enabling brain-wide electrophysiological tracking during development (Fig. 1a).

We restricted device implantation to the cranial neural plate, which forms the brain, avoiding the caudal region that extends axially to form the spinal cord. On the basis of our calculations, brain formation in frog embryos induces less than 30% axial strain on the device. Therefore, our initial design featured 40-nm-thick chromium (Cr)/gold (Au) serpentine interconnects and an 800-nm-thick SU-8 encapsulation layer, engineered to withstand 30% strain in organoids in vitro[22]. However, the significantly lower elastic modulus of frog embryos compared with organoids (Extended Data Fig. 1a) rendered SU-8 too stiff. It cut through the neural plate shortly after integration, critically damaging the embryo (Extended Data Fig. 1b,c).

The bending stiffness of each device layer is proportional to Ebh^3, where E, b and h are the elastic modulus, width and thickness, respectively. The SU-8 encapsulation layer dominated the overall device flexibility owing to its high thickness and modulus. We considered that using a softer dielectric layer would improve flexibility and reduce tissue damage. To test this, we designed a 1-µm-thick mesh structure using the elastomer styrene–ethylene–butylene–styrene (SEBS), which integrates into the neural tube during neurulation without visible damage (Extended Data Fig. 1d). However, SEBS is incompatible with submicrometre multilayer photolithography, limiting its applicability for fabricating stretchable mesh electronics.

We therefore developed a photoresist based on perfluoropolyether–dimethacrylate (PFPE–DMA), a material with low elastic modulus, intrinsic stretchability (Extended Data Fig. 1e,f) and chemical orthogonality with fabrication processes. By tuning the molecular weight of the PFPE–DMA precursor, we adjusted the modulus of the photopatterned film (Fig. 1d). More flexible PFPE–DMA films better matched brain tissue mechanics but reduced fabrication yield. We selected an 8-kDa PFPE–DMA formulation with a modulus of about 0.3 MPa (Extended Data Fig. 1e and Supplementary Discussion). For comparison, the moduli of the stage 15 embryo and brain tissue are 74.10 ± 2.45 Pa (mean ± s.e.m., $n = 100$) and about 1 kPa, respectively; whereas the moduli of SU-8 and SEBS are about 4 GPa (ref. 24) and about 17.65 MPa (ref. 25), respectively (Fig. 1e and Extended Data Fig. 1a). Cyclic tests confirmed that 8-kDa PFPE–DMA maintained stable linear elasticity over 50 cycles of 50% uniaxial stretching (Fig. 1f). PFPE–DMA-encapsulated Au serpentine ribbons also retained structure integrity under the same strain (Fig. 1g).

To assess the impact of device stiffness on embryonic brain implantation, we compared 1-µm-thick PFPE–DMA and SU-8 encapsulated 40-nm-thick Au serpentine ribbons using finite element analysis (FEA). When stretched to 29% strain, close to the relative extension of the *Xenopus* brain during early-stage development, the maximum stress in the PFPE–DMA ribbon was 68 kPa, whereas that in the SU-8 ribbon reached 759 MPa (Fig. 1h). Given the yield strengths of PFPE–DMA (0.45 MPa, ≫68 kPa; Extended Data Fig. 1e) and SU-8 (80 MPa (ref. 24), ≪759 MPa), the PFPE–DMA ribbon remained within its elastic deformation range, whereas the SU-8 ribbon probably failed. Further FEA showed that when stretched to the same maximum stress of 100 kPa, close to the limit of embryonic tissue tolerance[26], the PFPE–DMA ribbon reached 39.48% strain (Fig. 1i), exceeding embryonic axial deformation during development. In contrast, the SU-8 ribbon deformed only 0.0040%, indicating that it is too stiff to deform alongside the embryo. FEA of the interaction between each mesh and the embryonic neural plate during neurulation (Fig. 1j,k, Extended Data Fig. 2 and Methods) showed that PFPE–DMA meshes introduced a maximum force of about 0.1 µN and stress of about 10 Pa, whereas SU-8 meshes introduced a force of about 1 mN and stress of about 90 Pa. These results suggest that PFPE–DMA meshes introduce significantly less mechanical strain to the neural plate during implantation. In addition, implantation tests showed that SU-8 adhered to embryonic cells, scraping and dislodging them (Extended Data Fig. 1b). In contrast, PFPE–DMA showed lower surface free energy (Extended Data Fig. 1g) and a smaller contact angle with cytomembrane analogues (Extended Data Fig. 1h). Experiments confirmed that a 1-µm-thick PFPE–DMA stretchable mesh could be implanted into the embryonic brain without observable damage (Extended Data Fig. 1i).

We designed the PFPE–DMA mesh device to integrate seamlessly with the embryo during neurulation. During implantation, the embryo is gently positioned beneath the device (Fig. 2a and Extended Data Fig. 1j). Maintaining close contact between the electrode array and neural plate is crucial for ensuring full embedding into the neural tube as it forms. To achieve this, the device includes: (1) stretchable ribbons anchored to the wafer that secure the embryo and align the electrode array on the neural plate (Extended Data Fig. 1k); (2) blockers that prevent the device from contacting the caudal neural plate, which significantly elongates into the spinal cord—beyond the stretchability of the PFPE–DMA device (Extended Data Fig. 1l); and (3) face-down electrodes with fully encapsulated stretchable interconnects (Supplementary Fig. 1a and Supplementary Discussion), enabling direct electrical contact with neurons.

Fabrication of soft mesh electronics

We implemented PFPE–DMA as the encapsulation layer for a functional stretchable mesh device, adapting a photolithographic protocol to pattern multilayered, ultrathin PFPE–DMA structures (Fig. 2b,c and Methods). Key fabrication steps included: (1) preventing oxygen exposure during PFPE-DMA polymerization by enclosing the conventional mask aligner in a nitrogen chamber (Extended Data Fig. 3a–d); (2) improving surface adhesion for photopatterning and metal deposition by treating PFPE–DMA with argon gas plasma (Extended Data Fig. 3e,f and Supplementary Fig. 1b); and (3) patterning a platinum (Pt) electrode array as the bottom layer to ensure direct neuron contact during implantation (Fig. 2b,c and Extended Data Fig. 3g).

We evaluated the mechanical properties of the PFPE–DMA device. Photographic and bright-field microscopic images (Fig. 2d–h) confirmed successful patterning of PFPE–DMA passivation and Au interconnects with micrometre-scale resolution. Scanning electron microscopy (SEM; Extended Data Fig. 4a,b) and atomic force microscopy (AFM) topography (Extended Data Fig. 4c,d) showed smooth passivation surfaces free of cracks or defects. Cross-sectional SEM images (Fig. 2i–l) confirmed complete encapsulation of Au interconnects by

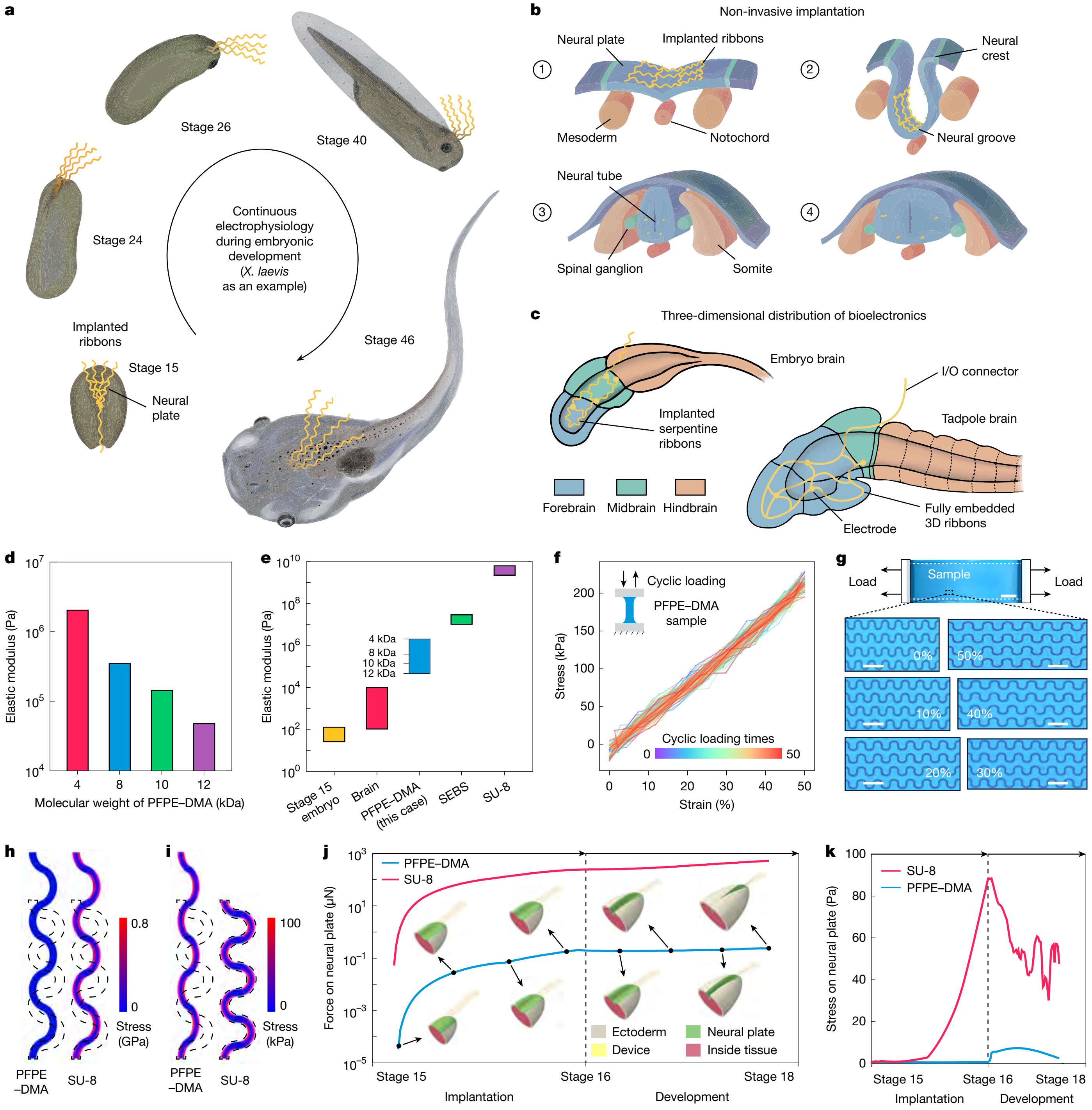

Fig. 1 | Tissue-level-soft bioelectronics for brain implantation via embryonic development. a, Schematics showing the stepwise implantation of soft mesh electronics into the *Xenopus* embryo brain via organogenesis. The electronics track brain-wide, continuous electrophysiological evolution throughout development. A stretchable electrode array is laminated onto the neural plate at the beginning of neurulation (stage 15). During neurulation, tissue reconfiguration embeds the mesh into the neural tube (stage 24), which deforms with the neural tube as it re-organizes into a 3D tadpole brain (stages 26, 40 and 46). **b**, Schematics of coronal views of neural plate development showing how the mesh electronics integrate non-invasively into the neural tube via neurulation. **c**, Schematics showing that expansion and folding of the neural tube fully distribute stretchable mesh electronics—externally connected via an input/output (I/O) connector—throughout the 3D structure of the brain. **d**, Elastic modulus of crosslinked PFPE–DMA with 4-kDa, 8-kDa, 10-kDa and 12-kDa molecular weight. **e**, Elastic modulus of stage 15 embryos, brain tissue, PFPE–DMA, SEBS and SU-8. **f**, Stress–strain curve of a representative 8-kDa PFPE–DMA film under 50 cycles of 50% uniaxial stretch loading. **g**, Photographic image of representative 8-kDa PFPE–DMA-encapsulated serpentine Au ribbons in a uniaxial stretch test. Scale bar, 2 mm. Zoomed-in views show the serpentine ribbons at 0%, 10%, 20%, 30%, 40% and 50% strain states. Scale bars, 100 μm. **h**,**i**, Stress distributions in PFPE–DMA and SU-8 serpentine ribbons when stretched to the same strain (**h**) and the same maximum von Mises stress (**i**). The dashed lines show the initial shapes of the ribbons. **j**,**k**, Simulations showing the force (**j**) and maximum von Mises stress (**k**) from the SU-8 and PFPE–DMA meshes applied to the neural plate during implantation and development from stages 15 to 18.

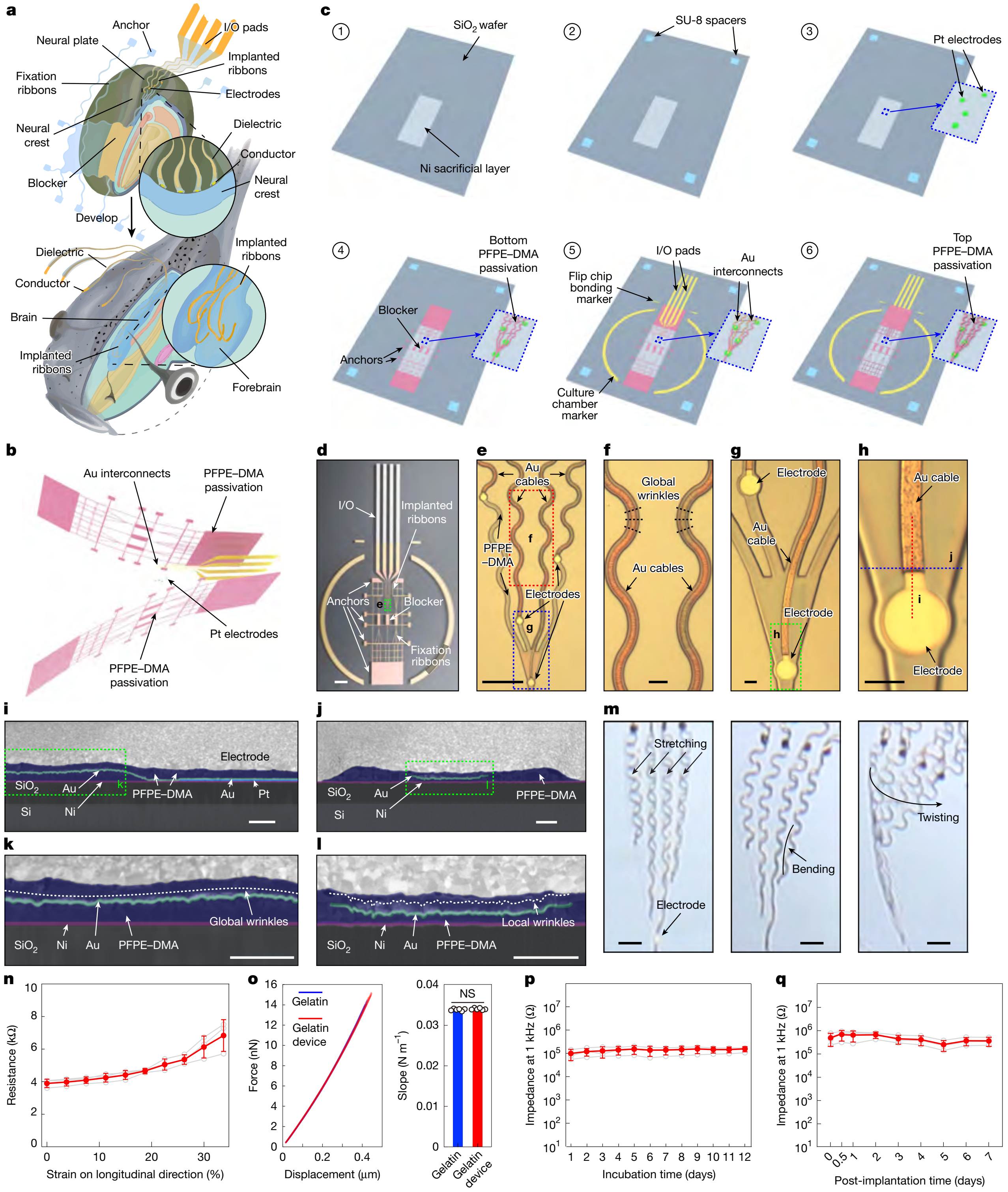

Fig. 2 | Fabrication of tissue-level-soft mesh electronics for embryo implantation. a, Schematics of mesh electronics designed for embryo implantation. **b**, Schematics showing trilayer structure of PFPE–DMA-encapsulated mesh electronics. **c**, Fabrication flow of the PFPE–DMA mesh electronics. Insets with blue dashed boxes show zoomed-in views of the electrode array. **d**, Photograph of a PFPE–DMA mesh electronics on glass substrate. **e**, Bright-field image of the green dashed box region in **d**. **f**,**g**, Bright-field images of the red (**f**) and blue (**g**) dashed box regions in **e**. **h**, Bright-field image of the green dashed box region in **g**. **i**–**l**, SEM images showing cross-sections of PFPE–DMA mesh electronics. Each layer is pseudo-coloured. **i**,**j**, SEM images showing cross-sections along the red (**i**) and blue (**j**) dashed lines in **h**. **k**, SEM image of the green dashed box region in **i**. **l**, SEM image of the green dashed box region in **j**. **k**,**l**, Dashed lines parallel to the Au layer indicate its global (**k**) and local (**l**) wrinkles. **m**, Photographs showing the free-floating mesh electrode array during stretching, bending and twisting tests. **n**, Electrode resistance as a function of strain in the stretch test. **o**, Left: force as a function of displacement in three-point bending tests of gelatin membrane and gelatin membrane embedded with mesh electronics. Right: statistics of curve slopes in the left plot. Bar plots indicate mean ± s.d.; each dot represents one sample; two-tailed unpaired *t*-test, $n = 6$; NS, not significant. **p**,**q**, Electrode impedance at 1 kHz as a function of incubation time in 37 °C PBS (**p**) and post-implantation time (**q**). In **n**, **p** and **q**, the red dots and line plots indicate mean ± s.d.; $n = 3$; each grey dot and line plot represents one sample. Scale bars, 1 mm (**d**), 100 μm (**e**,**m**), 10 μm (**f**–**h**), 1 μm (**i**–**l**).

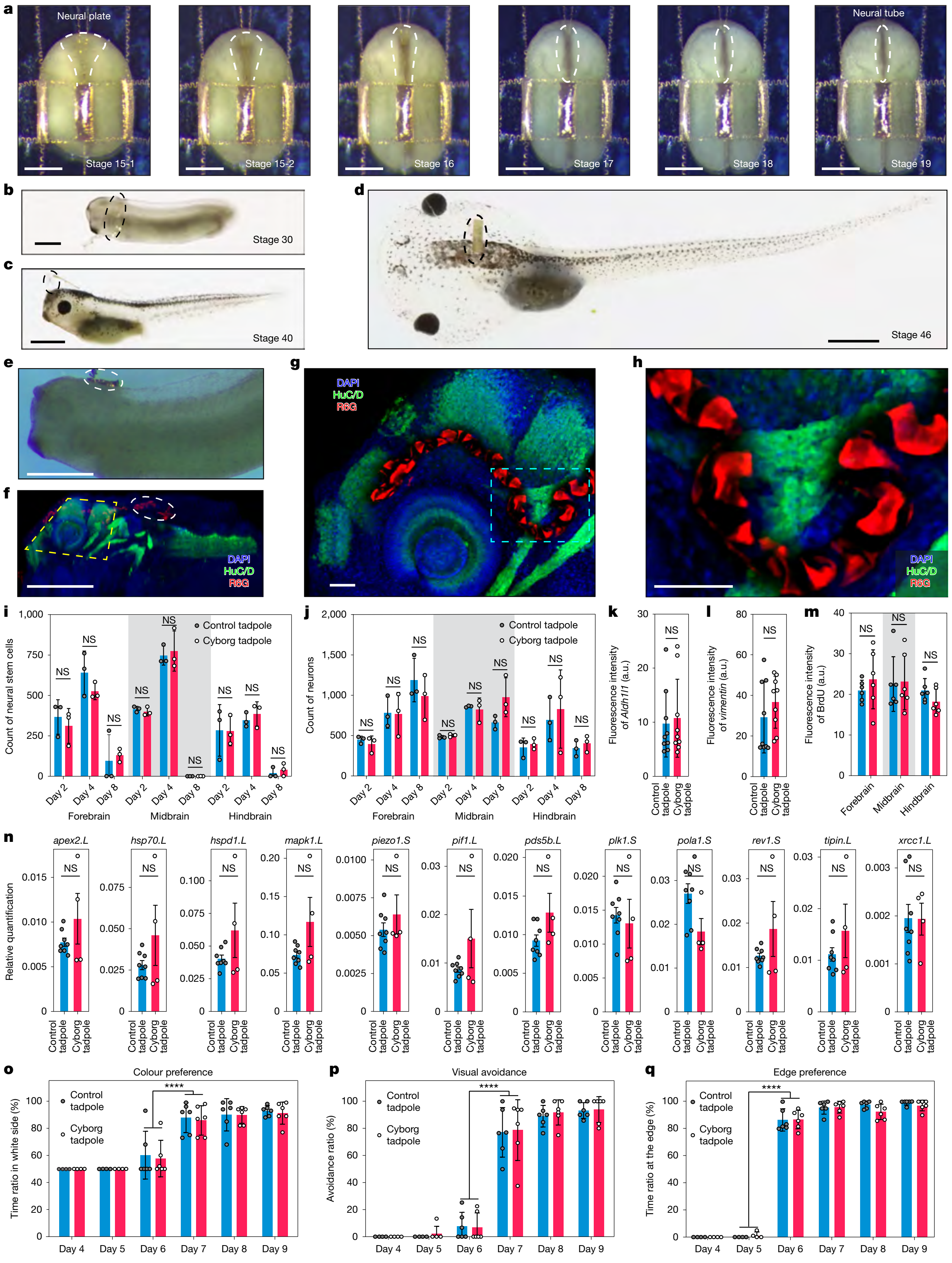

Fig. 3 | See next page for caption.

PFPE–DMA. Further characterizations indicated self-wrinkling of PFPE–DMA-encapsulated Au interconnects across multiple scales: anisotropic global wrinkles at the micrometre scale (Fig. 2j and Extended Data Fig. 4e) and isotropic local wrinkles at the submicrometre scale (Fig. 2l and Extended Data Fig. 4f,g). Together, these multi-scale wrinkles enhance the stretchability of the interconnects.

Fig. 3 | Minimally invasive brain implantation of tissue-level-soft mesh electronics via embryonic development. a, Time-lapse bright-field images of a frog embryo implanted with mesh electronics at different stages showing the gradual internalization of the electrode array (dashed circles) into the neural plate. **b**–**d**, Photographs of the embryo in **a** at stages 30 (**b**), 40 (**c**) and 46 (**d**). **e**,**f**, Photograph (**e**) and 3D reconstructed confocal fluorescence image (**f**) of a fixed cyborg tadpole. 4′,6-Diamidino-2-phenylindole (DAPI) labels the cell nuclei, rhodamine 6G (R6G) labels the device and HuC/D labels the neurons. In **b**–**f**, the dashed circles highlight the interconnects outside of the brain. **g**, Zoomed-in image of the yellow dashed box region in **f** showing electronics folded inside the neural tube. **h**, Zoomed-in image of the cyan dashed box region in **g** showing the interface between the embedded electronics and neurons. **i**–**m**, Bar and dot plots quantifying the number of neural stem cells (**i**) and neurons (**j**), and the fluorescence intensity of *Aldh1l1* (**k**), *vimentin* (**l**) and BrdU (**m**) in fluorescence images of the cryosection stained cyborg and control tadpoles. In **i**–**m**, the bar plots indicate mean ± s.d.; each dot represents one sample; two-tailed unpaired *t*-test; $n = 4$ (**i**,**j**) and $n \geq 8$ (**k**–**m**); NS, not significant. In **i**,**j**,**m**, grey shadings distinguish plots from different brain regions. a.u., arbitrary units. **n**, Bar and dot plots showing the stress gene expressions in cyborg and control tadpoles at stage 46. Bar plots indicate mean ± s.e.m.; each dot represents one sample; two-tailed unpaired *t*-test, $n \geq 4$; NS, not significant. **o**–**q**, Statistical analysis of colour preference (**o**), visual avoidance (**p**) and edge preference (**q**) behaviour test data from control and cyborg tadpoles at 4 to 9 DPF. Bar plots indicate mean ± s.d.; each dot represents a single trial; two-tailed unpaired *t*-test; $n \geq 8$; $^{****}P < 0.0001$. Scale bars, 500 µm (**a**), 1 mm (**b**–**f**), 100 µm (**g**,**h**).

Following fabrication, the device was released from the substrate (Extended Data Fig. 3h). The free-floating stretchable mesh remained intact when stretched, bent or twisted (Fig. 2m). SEM imaging confirmed that the device ribbons remained intact after deformation (Extended Data Fig. 4h–j). Impedance testing demonstrated that fully encapsulated interconnects maintained conductivity after bending and under 33% longitudinal or 38% transverse uniaxial strain (Fig. 2n and Extended Data Fig. 4k,l). A three-point bending test using AFM demonstrated that the device, when embedded in a 100-µm-thick gelatin membrane, introduced negligible additional force compared with gelatin alone (Fig. 2o and Methods), suggesting its tissue-level softness and stretchability.

We characterized the electrical performance and in vitro biocompatibility of stretchable electronics. Electrodes were electroplated with Pt-black to reduce electrochemical impedance for in vivo recording (Extended Data Fig. 4m). Impedance remained consistent across fabrication batches (Extended Data Fig. 4n). Continuous measurements showed stable impedance over 12 days of in vitro incubation (Fig. 2p) and 7 days of in vivo implantation (Fig. 2q). A 10-day in vitro co-culture of the PFPE–DMA and its potential degradation products with rat cortical neurons showed no significant change in the live/dead cell ratio (Extended Data Fig. 4o). These results confirm the longevity, stretchability and in vitro biocompatibility of the mesh electronics, supporting their use in in vivo implantation and electrophysiological studies throughout development.

Implantation via embryo development

We implanted PFPE–DMA-based mesh electronics into *Xenopus* embryos at the Nieuwkoop and Faber stage 15. Time-lapse bright-field imaging (Fig. 3a) showed the gradual internalization of the stretchable mesh electronics as the neural plate folded into the neural tube (stages 15 to 19). By stages 30–46 (Fig. 3b–d), the embedded meshes remained fully integrated with the developing brain without disrupting development. Three-dimensional confocal fluorescence imaging of whole-mount-stained cyborg tadpoles (Fig. 3e, Extended Data Fig. 5a and Methods) showed that the mesh electronics were embedded across multiple brain regions (Fig. 3f). Further images (Fig. 3g,h, Extended Data Fig. 5c and Supplementary Fig. 2) showed integration of the mesh within the forebrain, midbrain and hindbrain, with electrodes forming close contact with neurons. Cyborg tadpoles showed normal development through later stages, showing comparable morphology, survival rates and developmental timing to control tadpoles (Supplementary Fig. 3 and Supplementary Discussion).

When implantation was performed at a later stage of neurulation (stage 16), the device remained superficial to the neural tube rather than integrating within it (Extended Data Fig. 5d), highlighting the necessity of integration at the beginning of neurulation. We performed cell-type-specific protein marker staining on coronal brain sections from tadpoles at 2, 4 and 8 days post-fertilization (DPF; Extended Data Fig. 5b and Methods). Imaging confirmed successful integration of the device within the neural tissue (Extended Data Fig. 5e).

To assess the impact of embedded devices on cell proliferation, differentiation and potential immune responses, we analysed cell counts and fluorescence intensity (Supplementary Fig. 4) in cryosection images across developmental stages. No statistically significant differences were observed in neural stem cell or neuron counts between cyborg and control tadpoles (Fig. 3i,j). In addition, the fluorescence intensity of astrocyte markers aldehyde dehydrogenase 1 family member l1 (*Aldh1l1*) and *vimentin*[27], and the cell proliferation marker bromodeoxyuridine (BrdU)[28] showed no statistically significant differences at the implantation site between control and cyborg tadpoles (Fig. 3k–m and Methods), which are consistent with previous reports on in vivo implantation of flexible bioelectronics[17,19,21,29–33].

To examine potential stress responses, we performed quantitative polymerase chain reaction (qPCR) on cyborg and control embryos at 8 DPF. No significant changes were detected in the expression of key stress-related genes (Fig. 3n and Methods), suggesting minimal impact of the implanted device on embryonic development.

We further evaluated behavioural development in cyborg and control tadpoles using three well-established tests (Extended Data Fig. 6a–i and Methods). At 9 DPF, no statistically significant differences were found in: (1) colour preference (Extended Data Fig. 6j); (2) visual avoidance of moving black dots (Extended Data Fig. 6k); and (3) swimming behaviour along the container edge (Extended Data Fig. 6l). Daily evaluation from 1 DPF to 9 DPF showed no significant differences at any stage of development. Both cyborg and control tadpoles reached expected developmental milestones (Fig. 3o–q). Overall, these results suggest that the implanted devices did not significantly disrupt neural development, stress response or behaviour maturation in *Xenopus* tadpoles.

Neural tracking in *Xenopus* development

We tested whether the integrated electronics could continuously record neural activity during brain development (Extended Data Fig. 7a,b and Methods), benchmarking the signals against previous terminal measurements. Continuous recordings from the same embryo at different developmental timepoints captured the evolution of stage-specific electrical activities (Fig. 4 and Extended Data Fig. 7c). At stage 24, we recorded spontaneous slow oscillations from four electrodes distributed across different brain regions (Fig. 4a–c and Extended Data Fig. 7c–e). Activation time delays across channels (Fig. 4d,e and Methods) showed that these oscillation waves propagated consistently from the forebrain to the midbrain, suggesting synchronized brain-wide activity. At stage 26, faster calcium-wave-like signals emerged (Fig. 4f–h and Extended Data Fig. 8a,b). The waveform width and interval matched previously reported spontaneous localized calcium release events in cells[34] (Extended Data Fig. 7f,g). Cross-channel examination of the temporal dynamics of these fast waves did not reveal stable propagation delays, suggesting a gradual increase of localized

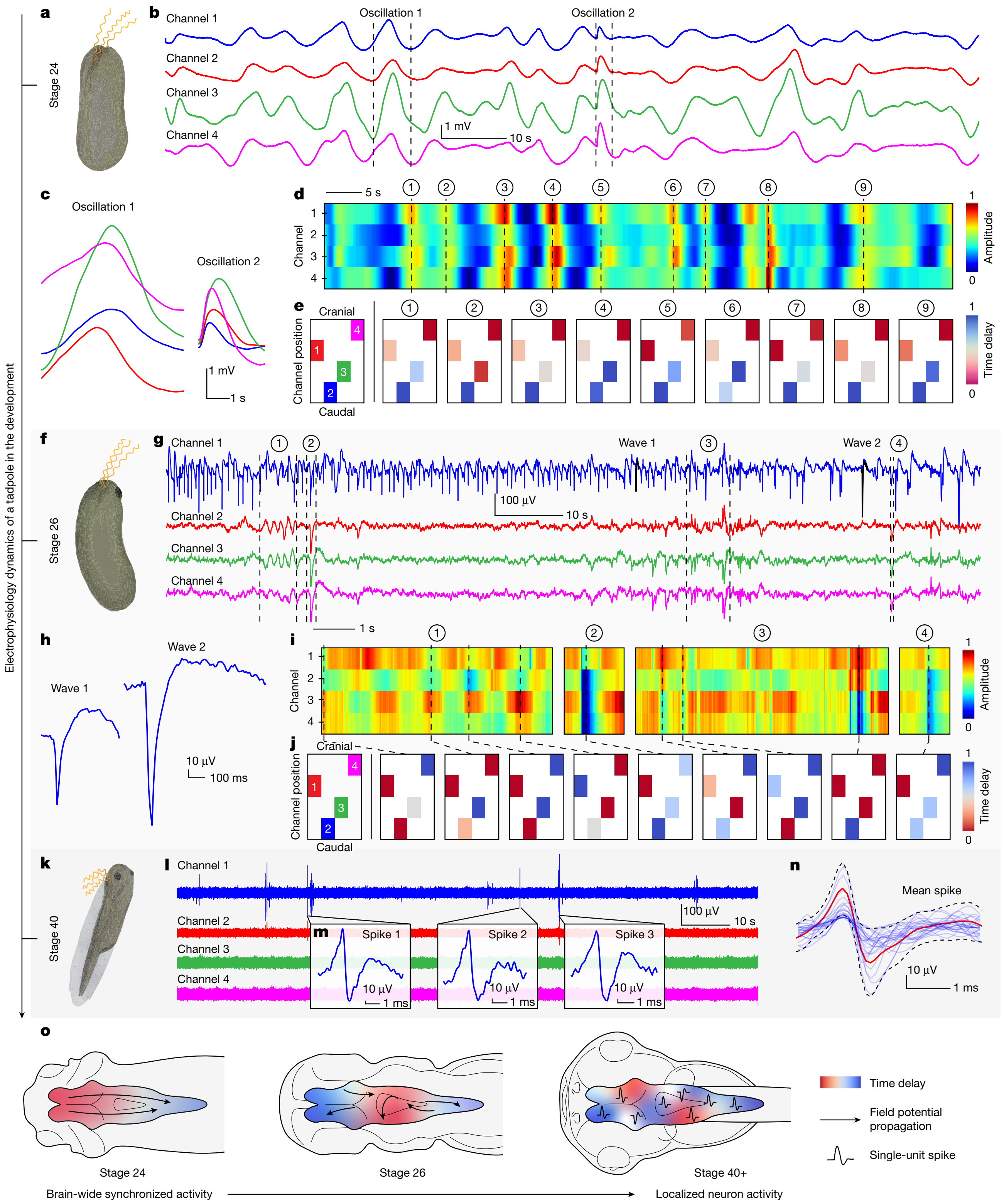

Fig. 4 | Continuous tracking of in vivo neural electrical activities from the same tadpole during organogenesis and brain development. a, Schematic of the cyborg tadpole at developmental stage 24. **b**, Representative voltage traces from four channels in the cyborg tadpole at stage 24. **c**, Zoomed-in views of the signals highlighted by dashed lines in **b**. **d**, Heat map of the amplitude of the signals as a function of time for the voltage traces in **b**. **e**, Spatiotemporal delay of signals across channels from the highlighted timepoints in **d**. The panel on the left illustrates the channel positions. **f**, Schematic of the cyborg tadpole at developmental stage 26. **g**, Representative voltage traces from four channels in the cyborg tadpole at stage 26. **h**, Zoomed-in views of the signals highlighted by dashed lines in **g**. **i**, Heat map of the amplitude of the signals as a function of time for the voltage traces in **g**. **j**, Spatiotemporal delay of signals across channels from the highlighted timepoints in **i**. The panel on the left illustrates the channel positions. **k**, Schematic of the cyborg tadpole at developmental stage 40. **l**, Voltage traces from four channels in the cyborg tadpole at stage 40. **m**, Three boxes showing zoomed-in views of representative single spikes in **l**. **n**, Mean spike waveform (mean ± s.d.) overlaid on all spike waveforms from the same sorted unit, derived from the data presented in **l**. **o**, Schematics illustrating how the neural activity evolves from brain-wide coordinated activity to localized neural activity and the emergence of single-unit spikes during *Xenopus* development.

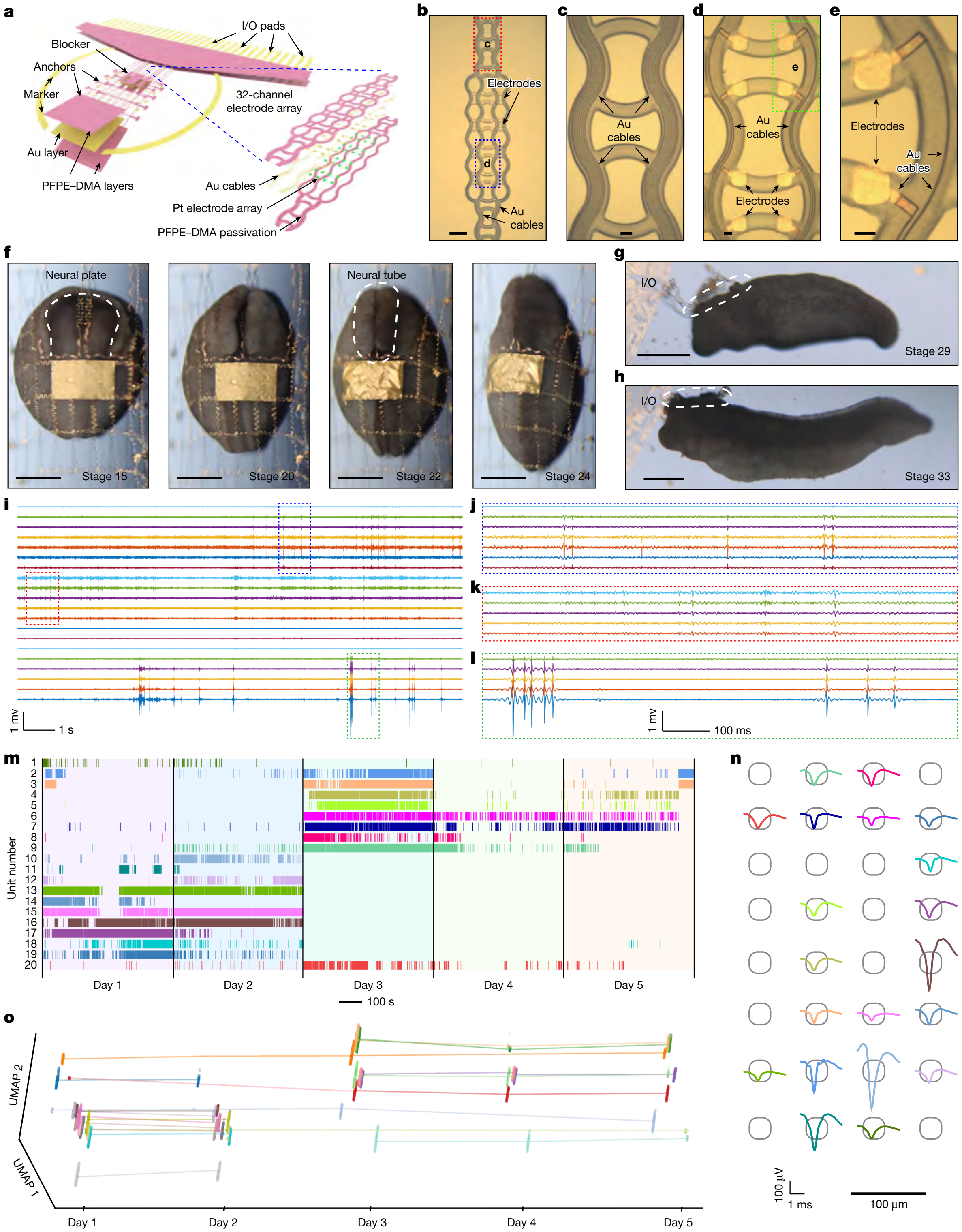

Fig. 5 | Tracking of single-unit action potential by soft and stretchable high-density mesh electrode array during axolotl embryonic brain development. **a**, Schematic showing the trilayer structure of a PFPE–DMA-encapsulated stretchable mesh electrode array: PFPE–DMA passivation layers sandwich Au interconnects for a high-density 32-channel electrode array. **b**, Bright-field image showing the high-density 32-channel electrode array for electrophysiological recording. **c**,**d**, Zoomed-in view of the red and blue dashed box regions in **b** showing the stretchable interconnects (**c**) and electrode array (**d**), respectively. **e**, Bright-field image of the zoomed-in view of the green dashed box region in **d** showing two individual electrodes. **f**, Time-lapse bright-field images of a representative axolotl embryo implanted with stretchable mesh electronics at different development stages, showing the stepwise internalization of the stretchable mesh electronics through the neural plate to neural tube transition (dashed lines). **g**,**h**, Bright-field images of the axolotl embryo implanted with stretchable mesh electronics at stages 29 (**g**) and 33 (**h**). The dashed circles highlight the interconnects outside of the brain. **i**, Representative filtered voltage traces (300–3,000-Hz bandpass filter) recorded in a cyborg axolotl embryo. **j**–**l**, Zoomed-in views of the voltage traces in **i** highlighted by the blue dashed box (**j**), red dashed box (**k**) and green dashed box (**l**). **m**, Raster plot of spikes sorted from continuous 5-day recording in the cyborg axolotl embryo. **n**, Average template over the extremum electrodes of units sorted from the continuous recording in **m**. **o**, UMAP plots across the continuous recording of sorted units in **n**. Scale bars, 100 μm (**b**), 10 μm (**c**–**e**), 1 mm (**f**–**h**).

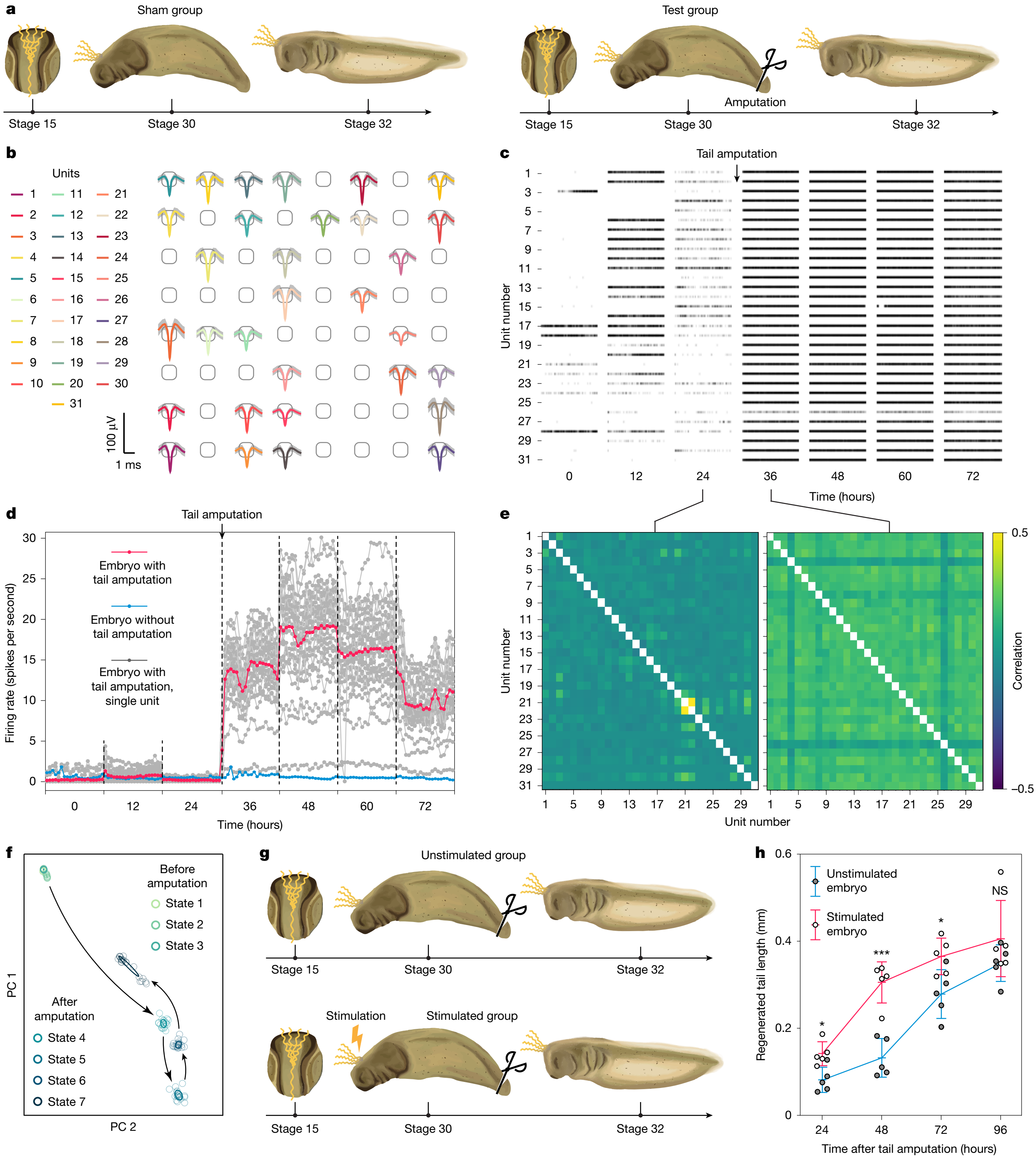

Fig. 6 | Investigating neural processing of distant injury and tail regeneration using high-density electrode arrays in late-stage axolotl embryos. **a**, Schematic illustration of the experiment designed to study neural signal changes in the axolotl brain following tail amputation and regeneration. **b**, Sorted unit (mean ± s.d.) at each electrode from a representative continuous recording following tail amputation and regeneration. **c**, Raster plot showing the activity units in **b** over the continuous recording. **d**, Firing rate changes of units in **b** throughout the recording. The grey dots and lines represent firing rate changes of individual units in the tail-amputated embryo. The red dots and lines represent the average firing rate changes of units in the tail-amputated embryo. The blue dots and lines represent average firing rate changes of units in the embryos without tail amputation. **e**, Pearson correlation coefficient of unit spike firing rate[46] recorded immediately before and after tail amputation. **f**, Neural states[47] across continuous recording derived from factor analysis of spike trains in **c**. Each state is represented with a solid covariance ellipse, plotted on semi-transparent epoch circles. **g**, Schematic illustration of the experiment designed to investigate tail regeneration with electrical stimulation from the brain-embedded electrodes. **h**, Comparison of tail regeneration length over time in cyborg axolotl embryo with and without electrical stimulation following tail amputation. Bar plots indicate mean ± s.d.; each dot represents one animal; two-tailed unpaired *t*-test; $n = 5$; *72 hours, $P = 0.0249$, *24 hours, $P = 0.0105$, ***$P = 0.0003$, NS, not significant.

brain activity (Fig. 4i,j and Methods). At stage 40, we detected both local field potential-like signals and fast spikes (Fig. 4k–m). A 300–3,000-Hz bandpass filter isolated single-unit action potential-like fast spikes using a conventional spike sorting algorithm (Fig. 4n and Methods). Action potential characteristics were comparable to previously reported data[35] (Extended Data Fig. 7h). Drug testing confirmed that these spikes originated from neuronal activity (Extended Data Fig. 8c–g). Imaging confirmed that electrodes recording action potential-like signals formed direct contact with neurons (Extended Data Fig. 8h–o).

Neural tracking in axolotl development

We significantly increased the number and density of electrodes while maintaining the mechanical properties required for embryo integration by employing electron-beam (e-beam) lithography to pattern nanometre-wide metal interconnects on the soft PFPE–DMA substrate (Extended Data Fig. 9a). This advancement enabled simultaneous recording of activity from the same neurons across multiple electrodes, improving spike sorting accuracy and allowing reliable neuronal tracking in developing tissues. PFPE–DMA showed robustness and compatibility with e-beam processing, enabling nanometre-resolution metal patterning. This allowed us to fabricate a 32-channel electrode array with 500-nm-wide Au interconnects sandwiched by PFPE–DMA dielectric layers (Fig. 5a). Bright-field imaging confirmed precise interconnect patterning (Fig. 5b–e) and mechanical testing showed that the high-density stretchable electrode array maintained resilience under stretching, bending or twisting (Extended Data Fig. 9b).

We used these stretchable high-density mesh electrode arrays to record brain development in axolotl embryos, a well-established model for studying development and regeneration owing to its ability to regenerate after injury, including its nervous system[36]. Implantation follows the same procedure as in *Xenopus*. Time-lapse bright-field images (Fig. 5f) showed the stepwise internalization of the mesh by the neural plate during neural tube formation. By stages 29 and 33, the stretchable meshes were fully embedded in the developing brain (Fig. 5g,h).

We demonstrated that these high-density electrode arrays can reliably track single-unit action potentials throughout axolotl development. Cyborg axolotl embryos were continuously recorded up to stage 37, with spike-like signals first emerging at stage 25. Neuronal activity was simultaneously recorded by multiple nearby electrodes[37,38] (Fig. 5i–l and Supplementary Fig. 5). Over the following 5 days (corresponding to stages 27, 28, 29, 31 and 33, respectively), we recorded spikes (Fig. 5m) from 20 well-isolated neurons distributed across multiple electrodes (Fig. 5n). Clusters were visualized using uniform manifold approximation and projection (UMAP; Fig. 5o). Overlaying average spike waveforms with the electrode array layout confirmed that the activity of each neuron was consistently recorded by multiple nearby electrodes, with amplitude variations reflecting neuron–electrode distances (Extended Data Fig. 10a). By mapping electrode position and corresponding waveform amplitudes, we estimated neuron location relative to the array[37,38], allowing us to track neuron position changes during brain development (Extended Data Fig. 9g–i).

We used the cyborg axolotl model to investigate neuronal activity changes following injury, specifically tail amputation and subsequent regeneration. At stage 30, cyborg axolotl embryos (Fig. 6a) underwent tail amputation, whereas the sham group remained uninjured. Continuous recordings (Fig. 6b,c and Extended Data Fig. 10b) showed that, following amputation, neuron firing rates (Fig. 6d) increased significantly compared with pre-amputation levels (Extended Data Fig. 10c,d), whereas sham embryos showed stable activity. Tail amputation also alters neural population dynamics. Post-amputation neurons showed higher correlated activity[39] (Fig. 6e), and factor analysis[40] (Fig. 6f) revealed shifts in neural states, with initial divergence followed by partially reversion. To test whether neural activity changes influence regeneration, we applied continuous external electrical stimulation through brain-embedded electrodes, mimicking post-amputation neural activity patterns. Stimulated embryos (Fig. 6g,h) showed significantly accelerated regeneration rates compared with non-stimulation controls. By day 4, differences diminished as regeneration nearly completed.

Discussion

We developed a tissue-level-soft, stretchable electronic system using PFPE–DMA as a soft passivation layer compatible with photolithography and e-beam lithography, enabling high-density electrode arrays for long-term single-unit tracking. By leveraging the brain's natural 2D-to-3D reconfiguration during development, our approach achieved high-yield integration with developing brains (Supplementary Table 3) without disrupting development, as confirmed by immunostaining, fluorescence imaging, gene expression analysis and behavioural testing. The implanted device provided stable, millisecond-resolution neural recordings throughout organogenesis, offering a method for soft electronics implantation in 3D developing tissues.

Recordings from frog embryos (Fig. 4o and Extended Data Fig. 8p–t) revealed a transition from synchronized, brain-wide activity to localized neural dynamics. In the axolotl embryo model, long-term neural tracking (Fig. 5i–o and Extended Data Fig. 9g–i) before and after tail amputation revealed distinct neural responses to distant injury (Fig. 6c–f). External electrical stimulation through brain-embedded electrodes accelerated tail regeneration (Fig. 6h), suggesting a possible role of brain activity in tissue regeneration[41,42].

This platform is designed to be broadly accessible to the research community. The device fabrication is based on conventional fabrication processes, requiring minimal adaptation. Users should pay attention to ensuring strong adhesion between the PFPE–DMA and Au layers, as detailed in our protocol. Furthermore, the system can be scaled to support higher electrode counts by e-beam lithography (Extended Data Fig. 9c–f) or implementation of multiplexing circuits[37]. Although this method was initially demonstrated in frogs and axolotls—both widely used in developmental biology owing to their short developmental timelines—the conserved nature of neural development suggests that this approach can be extended to mammalian systems. Preliminary tests confirmed that the devices' mechanical properties are compatible with mouse embryos and neonatal rats (Supplementary Figs. 6 and 7 and Methods) and future studies may explore in vitro embryonic culture[43] or in utero implantations[44]. In addition, we adapted head-fixation methods using agarose gel (Supplementary Fig. 8 and Methods) for awake, behaving animals. Future combination of this system with virtual-reality platforms[45] could provide a powerful tool for investigating behaviour- and sensory-specific brain activity during development.

Online content

Any methods, additional references, Nature Portfolio reporting summaries, source data, extended data, supplementary information, acknowledgements, peer review information; details of author contributions and competing interests; and statements of data and code availability are available at https://doi.org/10.1038/s41586-025-09106-8.

1. Sanes, D. H. et al. *Development of the Nervous System* (Academic Press, 2011).
2. Smith, J. L. & Schoenwolf, G. C. Neurulation: coming to closure. *Trends Neurosci.* **20**, 510–517 (1997).
3. Randlett, O. et al. Whole-brain activity mapping onto a zebrafish brain atlas. *Nat. Methods* **12**, 1039–1046 (2015).
4. Keller, P. J. & Ahrens, M. B. Visualizing whole-brain activity and development at the single-cell level using light-sheet microscopy. *Neuron* **85**, 462–483 (2015).
5. Alivisatos, A. P. et al. The brain activity map. *Science* **339**, 1284–1285 (2013).
6. Stringer, C. et al. Spontaneous behaviors drive multidimensional, brainwide activity. *Science* **364**, 255 (2019).
7. Fox, M. D. & Raichle, M. E. Spontaneous fluctuations in brain activity observed with functional magnetic resonance imaging. *Nat. Rev. Neurosci.* **8**, 700–711 (2007).

8. Ahrens, M. B., Orger, M. B., Robson, D. N., Li, J. M. & Keller, P. J. Whole-brain functional imaging at cellular resolution using light-sheet microscopy. *Nat. Methods* **10**, 413–420 (2013).
9. Hong, G. & Lieber, C. M. Novel electrode technologies for neural recordings. *Nat. Rev. Neurosci.* **20**, 330–345 (2019).
10. Jun, J. J. et al. Fully integrated silicon probes for high-density recording of neural activity. *Nature* **551**, 232–236 (2017).
11. Abbott, J. et al. A nanoelectrode array for obtaining intracellular recordings from thousands of connected neurons. *Nat. Biomed. Eng.* **4**, 232–241 (2020).
12. Chiang, C. H. et al. Development of a neural interface for high-definition, long-term recording in rodents and nonhuman primates. *Sci. Transl. Med.* **12**, eaay4682 (2020).
13. Musk, E. An integrated brain–machine interface platform with thousands of channels. *J. Med. Internet Res.* **21**, e16194 (2019).
14. McDole, K. et al. In toto imaging and reconstruction of post-implantation mouse development at the single-cell level. *Cell* **175**, 859–876 (2018).
15. Kasthuri, N. et al. Saturated reconstruction of a volume of neocortex. *Cell* **162**, 648–661 (2015).
16. Pijuan-Sala, B. et al. A single-cell molecular map of mouse gastrulation and early organogenesis. *Nature* **566**, 490–495 (2019).
17. Liu, J. et al. Syringe-injectable electronics. *Nat. Nanotechnol.* **10**, 629–636 (2015).
18. Tian, B. et al. Macroporous nanowire nanoelectronic scaffolds for synthetic tissues. *Nat. Mater.* **11**, 986–994 (2012).
19. Xie, C. et al. Three-dimensional macroporous nanoelectronic networks as minimally invasive brain probes. *Nat. Mater.* **14**, 1286–1292 (2015).
20. Dai, X., Zhou, W., Gao, T., Liu, J. & Lieber, C. M. Three-dimensional mapping and regulation of action potential propagation in nanoelectronics-innervated tissues. *Nat. Nanotechnol.* **11**, 776–782 (2016).
21. Fu, T. M. et al. Stable long-term chronic brain mapping at the single-neuron level. *Nat. Methods* **13**, 875–882 (2016).
22. Li, Q. et al. Cyborg organoids: implantation of nanoelectronics via organogenesis for tissue-wide electrophysiology. *Nano Lett.* **19**, 5781–5789 (2019).
23. Le Floch, P. et al. Stretchable mesh nanoelectronics for 3D single-cell chronic electrophysiology from developing brain organoids. *Adv. Mater.* **34**, 2106829 (2022).
24. Xu, T. et al. Characterization of the mechanical behavior of SU-8 at microscale by viscoelastic analysis. *J. Micromech. Microeng.* **26**, 105001 (2016).
25. Gupta, P., Bera, M. & Maji, P. K. Nanotailoring of sepiolite clay with poly [styrene-b-(ethylene-co-butylene)-b-styrene]: structure–property correlation. *Polym. Adv. Technol.* **28**, 1428–1437 (2017).
26. Chanthasopeephan, T., Desai, J. P. & Lau, A. C. W. Study of soft tissue cutting forces and cutting speeds. *Stud. Health Technol. Inform.* **98**, 56–62 (2004).
27. Spruiell Eldridge, S. L. et al. A focal impact model of traumatic brain injury in *Xenopus* tadpoles reveals behavioral alterations, neuroinflammation, and an astroglial response. *Int. J. Mol. Sci.* **23**, 7578 (2022).
28. Yoshino, J. & Tochinai, S. Successful reconstitution of the non-regenerating adult telencephalon by cell transplantation in *Xenopus laevis*. *Dev. Growth Differ.* **46**, 523–534 (2004).
29. Khodagholy, D. et al. NeuroGrid: recording action potentials from the surface of the brain. *Nat. Neurosci.* **18**, 310–315 (2015).
30. Yang, X. et al. Bioinspired neuron-like electronics. *Nat. Mater.* **18**, 510–517 (2019).
31. Liu, Y. et al. Soft and elastic hydrogel-based microelectronics for localized low-voltage neuromodulation. *Nat. Biomed. Eng.* **3**, 58–68 (2019).
32. Minev, I. R. et al. Electronic dura mater for long-term multimodal neural interfaces. *Science* **347**, 156–163 (2015).
33. Kozai, T. D. Y. et al. Ultrasmall implantable composite microelectrodes with bioactive surfaces for chronic neural interfaces. *Nat. Mater.* **11**, 1065–1073 (2012).
34. Manita, S. & Ross, W. N. Synaptic activation and membrane potential changes modulate the frequency of spontaneous elementary Ca^{2+} release events in the dendrites of pyramidal neurons. *J. Neurosci.* **29**, 7833–7845 (2009).
35. Ciarleglio, C. M. et al. Multivariate analysis of electrophysiological diversity of *Xenopus* visual neurons during development and plasticity. *Elife* **4**, e11351 (2015).
36. Maden, M. Salamanders as key models for development and regeneration research. *Methods Mol. Biol.* **2562**, 1 (2023).
37. Steinmetz, N. A. et al. Neuropixels 2.0: a miniaturized high-density probe for stable, long-term brain recordings. *Science* **372**, eabf4588 (2021).
38. Schoonover, C. E., Ohashi, S. N., Axel, R. & Fink, A. J. P. Representational drift in primary olfactory cortex. *Nature* **594**, 541–546 (2021).
39. Denker, M., Yegenoglu, A. & Grün, S. Collaborative HPC-enabled workflows on the HBP Collaboratory using the Elephant framework. *Neuroinformatics* **19**, FZJ-2018-04114 (2018).
40. Cowley, B. et al. DataHigh: graphical user interface for visualizing and interacting with high-dimensional neural activity. *J. Neural Eng.* **10**, 066012–066019 (2013).
41. Wei, X. et al. Single-cell stereo-seq reveals induced progenitor cells involved in axolotl brain regeneration. *Science* **377**, eabp9444 (2022).
42. Lust, K. et al. Single-cell analyses of axolotl telencephalon organization, neurogenesis, and regeneration. *Science* **377**, eabp9262 (2022).
43. Takahashi, M. & Osumi, N. The method of rodent whole embryo culture using the rotator-type bottle culture system. *J. Vis. Exp.* **42**, 2170 (2010).
44. Huang, Q. et al. Intravital imaging of mouse embryos. *Science* **368**, 181–186 (2020).
45. Jouary, A., Haudrechy, M., Candelier, R. & Sumbre, G. A 2D virtual reality system for visual goal-driven navigation in zebrafish larvae. *Sci. Rep.* **6**, 34015 (2016).
46. Le Floch, P. et al. 3D spatiotemporally scalable in vivo neural probes based on fluorinated elastomers. *Nat. Nanotechnol.* **19**, 319–329 (2024).
47. Fowkes, F. M. Attractive forces at interfaces. *Ind. Eng. Chem.* **56**, 40–52 (1964).

Methods

Chemicals and materials

All chemicals were obtained from Sigma-Aldrich unless otherwise mentioned and used without further purification. PFPE precursors were obtained from Axoft or Solvay. SEBS was obtained from Asahi Kasei. All photoresists and developers were obtained from Kayaku Advanced Materials unless otherwise mentioned and used without further purification. PFPE–DMA precursors were prepared using previously reported methods[31,46].

Fabrication of stretchable mesh electronics

SU-8 devices. (1) Wafer cleaning: a 3-inch thermal oxide silicon wafer (2005, University Wafer) was rinsed with acetone, isopropyl alcohol (IPA) and water, then blown dry and baked at 110 °C for 3 min, followed by O_2 plasma treatment at 100 W, 40 standard cubic centimetres per minute (sccm) O_2 for 30 s. (2) Nickel (Ni) sacrificial layer: hexamethyldisilazane was spin-coated at 4,000 rpm for 1 min. LOR 3A was spin-coated at 4,000 rpm for 1 min and hard-baked at 180 °C for 5 min. S1805 was spin-coated at 4,000 rpm for 1 min and hard-baked at 115 °C for 1 min. Then the photoresists were exposed to 40 mJ cm^{-2} ultraviolet light and developed with CD 26 for 50 s, rinsed with deionized water and blown dry. After preparing the photoresist pattern, a 100-nm Ni layer was thermally deposited on the wafer (Sharon) and lifted off in Remover PG for 3 h. (3) Pt layer: 5/40 nm Cr/Pt layers were deposited by an e-beam evaporator (Denton) with photoresist and lifted off in Remover PG for 2 h. (4) Bottom SU-8 passivation layer: SU-8 2000.5 was spin-coated at 4,000 rpm for 1 min and pre-baked at 60 °C for 1 min and 95 °C for 1 min. SU-8 was exposed to 200 mJ cm^{-2} ultraviolet light, then post-baked at 60 °C for 1 min and 95 °C for 1 min. SU-8 was then developed in an SU-8 developer for 1 min, rinsed with IPA and blown dry. Finally, SU-8 was hard-baked at 180 °C for 1 min. (5) Au interconnects: 5/50/5 nm Cr/Au/Cr layers were deposited on the top of the bottom SU-8 passivation layer by an e-beam evaporator (Denton) with S1805 and lifted off in Remover PG for 8 h. (6) Top SU-8 passivation layer: the fabrication of the top SU-8 layer followed the same procedure as for the fabrication of the bottom SU-8 layer.

PFPE–DMA devices by photolithography. (1) Wafer cleaning and the preparation of the Ni sacrificial layer and Pt layer followed the same procedure as the fabrication of the SU-8 devices. (2) SU-8 spacers: SU-8 2010 was spin-coated on the wafer at 4,000 rpm for 1 min and pre-baked at 60 °C for 2 min and 95 °C for 2 min. SU-8 was exposed to 200 mJ cm^{-2} ultraviolet light, then post-baked at 60 °C for 2 min and 95 °C for 2 min. Finally, SU-8 was developed in an SU-8 developer for 2 min, rinsed with IPA and blown dry. (3) Bottom PFPE–DMA passivation layer: the wafer was first cleaned with acetone, IPA and water, and blown dry. Then the PFPE–DMA precursor was spin-coated at 3,000 rpm for 1 min and pre-baked at 115 °C for 2 min. The PFPE–DMA was patterned with 80 mJ cm^{-2} ultraviolet light in a custom nitrogen chamber, post-baked at 115 °C for 2 min, developed in developer (1:3 bis(trifluoromethyl) benzene/1,1,1,3,3-pentafluorobutane) for 1 min and blown dry. Finally, the PFPE–DMA pattern was hard-baked at 150 °C for 50 min. (4) Au interconnects: the PFPE–DMA surface was activated with inert gas plasma for 5 min. Then the photoresists, hexamethyldisilazane, LOR 3A and S1805 were patterned on the wafer as described in the preparation of the Ni sacrificial layer. After that, adhesion metal aluminium was sputtered at 250 W, 40 sccm argon for 90 s. Au was sputtered at 125 W, 40 sccm argon for 3 min (AJA International). Finally, the metal layers were lifted off in Remover PG overnight. (5) Top PFPE–DMA passivation layer: fabrication of the top PFPE–DMA layer followed the same procedure as for the fabrication of the bottom PFPE–DMA layer.

PFPE–DMA devices by e-beam photolithography. The e-beam fabrication process of PFPE–DMA stretchable mesh electronics followed the same protocol as mentioned above, except for the application of e-beam lithography to pattern Au interconnects on the bottom PFPE–DMA layer. Specifically, after the PFPE–DMA surface was activated using inert gas plasma for 5 min, the e-beam resist methyl methacrylate EL7 was spin-coated at 4,000 rpm for 1 min and then hard-baked at 150 °C for 90 s. Next, the e-beam resist 950 polymethyl methacrylate A6 was spin-coated at a rate of 4,000 rpm for 1 min and then hard-baked at 180 °C for 90 s. A 10-nm layer of Au was sputtered (AJA International) to assist the e-beam lithography process on the PFPE–DMA. The e-beam resists were patterned at 1,000 μC cm^{-2} (Elionix ELS-HS50). The Au layer was then removed using Au etchant, and the resists were developed (1:3 methyl isobutyl ketone/IPA) for 1 min. Final steps included sputtering adhesion metal aluminium at 250 W, 40 sccm argon for 90 s, and Au at 125 W, 40 sccm argon for 3 min (AJA International). The process was completed with an overnight lift-off of the metal layers in Remover PG.

Characterizations

Statistical analysis. All statistical tests performed were two-tailed, unpaired *t*-tests unless specified otherwise; actual *P* values are reported in Supplementary Table 1.

Three-point bending test. Ten grams per millilitre of gelatin (G1890) was dissolved in 60 °C deionized water. The gelatin solution was then cooled to 25 °C to form a thin membrane. PFPE–DMA mesh electronics were laminated on the membrane. Additional gelatin solution was added and cooled to embed the mesh electronics. Gelatin membranes were adhered over a 1-mm-wide gap on 3D-printed plastic substrates. An AFM cantilever (BRUKER, SAA-SPH-1UM) was loaded onto the centre of the samples over the gap. The force and displacement of the cantilever were recorded.

Elastic modulus measurement. The contact mode of an AFM (JPK Nanowizard AFM) was used to measure the elastic modulus of *Xenopus* embryonic tissue and organoids. Embryonic tissues were tested in 0.1 × MMR (a 1 l H_2O solution containing 5.844 g NaCl (S7653), 0.1492 g KCl (P3911), 0.1204 g $MgSO_4$ (M7506), 0.2940 g $CaCl_2$ (C1016), 1.192 g 4-(2-hydroxyethyl)-1-piperazineethanesulfonic acid (H3375), 200 mg gentamicin (VWR International, 0304), and 100 mg NaOH (S8045)), and brain and cardiac organoids were tested in 1× phosphate-buffered saline (PBS; VWR international, 97063-660). Samples were secured using custom 3D-printed parts specifically designed to fit the sample shape and maintain stability during measurements. The AFM cantilever (BRUKER, SAA-SPH-1UM) was loaded to record the force and displacement for the calculation of the elastic modulus.

Contact angle and surface free energy. Contact angles for various liquids (water, diiodomethane (158429) and phospholipid (P3817)) were measured through contact-angle measurement techniques. Images were analysed by using Fiji (version 2.9.0) to determine the contact angle. The surface free energy of each substrate was calculated from the contact angles of water and diiodomethane using the Fowkes model[47].

In vitro biocompatibility test. The PFPE–DMA mesh electronics were heated at 80 °C in a 1 M NaOH solution for 2 h to obtain its potential degradation products. After being washed by deionized water 10 times to remove the NaOH solution, PFPE–DMA devices or degradation products were mixed with the culture medium at a concentration of 1% v/v and co-cultured with wild-type rat cortical neurons for 10 days. The live cell ratio of the neurons was compared with the control using a cell viability and cytotoxicity assay (CELL BIOLABS, CBA-240).

Animal experiments

Frog embryos were obtained from the National Xenopus Resource. The correlation between developmental time (DPF) and the developmental stages of frog embryos follows the well-established database[48]. Axolotl embryos were obtained from the University of Kentucky (AGSC_100E). Mouse embryos were collected from pregnant 6-month-old C57BL/6 female mice (Charles River Laboratories) based on previous reports[49,50]. Neonatal rats were bred from pregnant 6-month-old female CD rats (Charles River Laboratories) following previously reported protocols[51]. Mice were housed under standard laboratory conditions with a 12-h light–dark cycle, at an ambient temperature of 20–26 °C and a relative humidity of 30–70%.

No statistical method was used to predetermine the sample size. Sample sizes for each experiment were selected based on commonly accepted standards in the field and to ensure reproducibility across multiple independent replicates.

The randomization is not applicable to the experiments because the experimental designs did not involve treatment allocation across different experimental groups. All samples were subjected to identical conditions, and comparisons were made between clearly defined biological or experimental categories (test group versus control group).

Blinding was not used. Measurements and data reported are quantitative and did not require subjective judgement from the investigators.

Ethics statement. All animal experimental procedures were approved by the Institutional Animal Care and Use Committee of Harvard under animal protocols 19-01-344-1 and 19-03-348-1.

Device assembly and treatment for implantation. (1) Wafer was cut using a dicing saw, protected by photoresist S1813 during the cutting process, and the photoresist was removed afterwards. (2) A flexible flat cable (Molex) was bonded to the input/output (I/O) pads using a flip-chip bonder (Finetech Fineplacer). (3) A microscope slide (VWR International, 48300-026) was used as a stable base, adhered to the wafer piece with low-toxicity silicone adhesive (World Precision Instruments, KWIK-SIL). A 50-ml centrifuge tube (VWR International, 525-0610) was cut to serve as the culture chamber and attached to the wafer piece with the same silicone adhesive. (4) The device was released from the substrate by removing the Ni sacrificial layer in Ni etchant (TFB, Transene), which was subsequently washed out using deionized water 10 times. The device was then incubated with 1 ml 0.01% poly-D-lysine hydrobromide solution (P4832) overnight. (5) The device was washed with deionized water 3 times and then incubated with 1 ml of 10 mg ml^{-1} culture-media-diluted Matrigel (Corning, 08-774-552). The culture media for frog embryos was 0.1× MMR; for axolotl embryos it was 1× Steinberg's solution (a 1 l H_2O solution containing 0.34 g NaCl, 0.005 g KCl, 0.008 g $Ca(NO_3)_2 \cdot 4H_2O$ (C2786), 0.01025 g $MgSO_4$ (M2643), 0.056 g Tris-HCl (10812846001) and 0.001 g phenol red (P3532)); for mouse embryos it was rat serum prepared as in previous reports[49,50].

Device implantation in frog and axolotl embryos. (1) De-jellying: frog embryos need de-jellying before implantation. Embryos were placed in a de-jelly solution (60 ml 1× MMR containing 1.2 g L-cysteine (168149) and 0.1 g NaOH) for 5 min and then washed with 1× MMR 5 times. (2) Device implantation: a stage 15 embryo was placed inside the culture chamber under a stereoscope. Next, the vitelline membrane of the embryo was peeled off using #5 tweezers (Fine Science Tools, 11252-40) to expose the neural plate. The embryo was then slid under the stretchable device using tweezers, ensuring that the implanted ribbons accurately overlapped with the neural plate. During this process, one tweezer held the device and another guided the embryo into position underneath.

Device implantation in mouse embryos. Before device implantation, the culture well plate was transferred from the incubator to a 37 °C heating pad. A pre-sterilized wafer piece carrying the anchored device was immersed in the media. Then the embryo was placed on the wafer, lying on its side with the neural plate facing the device. Using tweezers, the device was carefully elevated. Subsequently, the embryo was gently pushed towards the device to implant the device into the neuropore. Finally, the anchor was cut and the wafer piece was gently removed. The entire process needed to be completed within 10 min, and the embryos were promptly returned to culture immediately after implantation. The culture protocol of mouse embryos was adapted from previous reports[49,50].

Stereotactic device implantation in neonatal rats. Rat pups were kept on a regular 12-h light–dark cycle and housed with their mother before surgery. Pups underwent device implantation at postnatal days 5–7. They were placed on a customized platform for head fixation and were maintained under anaesthesia with 0.5% isoflurane during surgery. For device implantation, a circular piece of skin on the skull was cut away with surgical scissors. Then, a small cranial window was opened, and the probe was stereotactically advanced until all electrodes were inserted below the pial surface. A 100-µm-thick stainless-steel wire (A-M SYSTEMS, 793100) was partially inserted to the window as the ground. The device's I/O and the ground were carefully sealed and fixed with dental cement. After device implantation, the rat pups were placed back with their mother. Post-operative care was provided. Carprofen should be administered to rat pups for the following 4 days, both in the morning and in the afternoon. Activity, incision and pain were monitored and recorded daily after implantation.

Behaviour tests of frog tadpoles. Tadpoles for behaviour tests were cultured at room temperature on a white base under a 12-h day–night cycle. Behaviour tests were conducted between 13:00 and 16:00. For each trial, a tadpole was placed at the centre of a clear-bottomed round tank (diameter of 12 cm) filled to 5 cm with 0.1× MMR. The tank was positioned on a horizontal screen and covered in a dark box. The luminance of the screen was set to 50 cd m^{-2} when displaying the white colour. For cyborg tadpoles, a flexible cable connected the electrode array to the I/O on the wafer for data collection. Once the cable was detached from the I/O, cyborg frog tadpoles could swim freely with the embedded device.

Three behaviour tests were applied to the tadpoles: (1) colour preference to characterize the visual function based on the preference of frog tadpoles to stay on the white side of a bicoloured tank[52]; (2) visual avoidance to characterize the maturation of visual responses in the optic tectum based on the ability of tadpoles to avoid incoming obstacles[53]; and (3) edge preference to test the motor behaviour of tadpoles based on their preference and ability to move along the edge of a container[54]. During the test, the tadpole was stimulated by the appropriate pattern shown on the screen. In the colour preference test, the screen alternated between displaying half white and half black for 40 s each. In the visual avoidance test, a black dot was moved towards the tadpole on the screen. In the edge preference test, the tadpole swam freely on the white screen. The tadpole's response was video recorded by a camera positioned on top of the dark box. Any disturbances, including vibrations, light and sounds, needed to be avoided.

Whole-mount staining of cyborg frog tadpoles. Whole-mount staining[55] was applied to the tadpole to ensure that the brain–electronics system remained intact throughout imaging. (1) Fixation and bleaching: tadpoles were fixed with 4% paraformaldehyde (PFA; Thermo Fisher Scientific, J19943-K2) overnight at 4 °C and then transferred to a glass dish containing a bleaching solution (1.5 ml 30% H_2O_2 (H1009), 2 ml formamide (47670), 1 ml 20× SSC buffer to 35 ml deionized water). The dish was placed on a nutator over aluminium foil reflective backing and under fluorescent light. To remove bubbles caused by bleach, embryos were dehydrated in methanol for 5 min. Subsequently, the embryos were rehydrated over the course of 10 min in stages of 80% methanol/20% deionized water, 50% methanol/50% PBS and 20% methanol/80% PBS. (2) Staining (Supplementary Table 2): embryos were washed with 0.1% PBST (50 ml PBS contains 50 µl Triton X-100 (X100-1L)) twice, 30 min per wash. Then they were incubated in diluted CAS-Block (13.5 ml PBS containing 1.5 ml CAS-Block (Thermo Fisher Scientific, 008120)) for 1 h at room temperature. After that, tadpoles were stained in primary antibody solution (1 ml CAS-Block containing 10 µl anti-acetylated tubulin (T7451) and 10 µl 1:100 anti-HuC/D (Abcam ab184267)) for 2 days at 4 °C. Then the embryos were washed with PBST for 30 min at room temperature and then blocked in PBST-CAS for 30 min at room temperature. Subsequently, the embryos were incubated in secondary antibody solution (1 ml CAS-Block containing 2 µl 1:500 Alexa Fluor 488 (Invitrogen, A-11006), 2 µl 1:500 Alexa Fluor 594 (Invitrogen, A-11012), 20 µl 1:50 Alexa Fluor 647 Phalloidin (Thermo Fisher Scientific, A22287) and 1 µl 1:1000 DAPI (D9542)) for 2 days at 4 °C. Finally, the embryos were washed with PBST for 1 h at room temperature and then washed with PBS overnight at 4 °C. (3) Imaging: stained tadpoles were imaged in a homemade chamber. A 2-mm layer of vacuum grease (Z273554) was applied at the edge of a microscope slide to form the walls of a chamber. A tadpole was placed in the middle of the microscope slide and embedded in the mounting medium (Vector, H-1900). A cover glass was placed on the top of the vacuum grease to seal the chamber. The tadpole was positioned upside down on the confocal microscope (Leica, dMi8) and imaged with 5-µm stacks. All the images were stitched and processed with Fiji (version 2.9.0).

Cryosection staining of frog tadpoles. Inflammation markers were selected based on the following criteria: (1) their use in well-established studies related to *X. laevis*, and (2) their documentation in the *X. laevis* gene expression database[48]. (1) Fixation: tadpoles were fixed with 4% PFA overnight at 4 °C and then incubated in 0.1% PBST overnight at 4 °C, followed by incubation in 0.1% PBST containing 15% gelatin (G1890)/15% sucrose (S7905) overnight at 40 °C. Subsequently, the tadpoles were frozen in the gelatin/sucrose solution at −80 °C overnight for cryosection. (2) Staining (Supplementary Table 2): slides were placed in a wet box and incubated at 40 °C to remove residual gelatin/sucrose solution. Then the slides were washed with 0.1% PBST for 15 min at room temperature and incubated in blocking buffer (20 ml 0.1% PBST containing 0.2 ml donkey serum (Jacksonimmuno, 017-000-121) and 0.8 g bovine serum albumin (Thermo Fisher Scientific, BP1600-100)) for 1 h at room temperature. Subsequently, slides were incubated in primary antibody solution overnight at 4 °C. Slides were then washed with 0.1% PBST 3 times and incubated in secondary antibody solution overnight at 4 °C. Finally, the slides were washed with 0.1% PBST 3 times and sealed. Primary antibody solution for Sox2, Myt1 and acetylated tubulin staining: 2 ml blocking buffer containing 20 µl 1:100 anti-Sox2 (Invitrogen, 14-9811-82), 20 µl 1:100 anti-Myt1 (Abcam, ab251682) and 20 µl 1:100 anti-acetylated tubulin (T7451). Secondary antibody solution for anti-Sox2, anti-Myt1 and anti-acetylated tubulin staining: 4 ml blocking buffer containing 8 µl 1:500 Alexa Fluor 488 (Invitrogen, A-11006), 8 µl 1:500 Alexa Fluor 594 (Invitrogen, A-11012), 8 µl 1:500 Alexa Fluor 647 (Invitrogen, A-32787) and 4 µl 1:1000 DAPI (D9542). Primary antibody solution for BrdU staining: 2 ml blocking buffer containing 20 µl 1:100 BrdU monoclonal antibody (Invitrogen, B35128). Secondary antibody solution for BrdU staining: 4 ml blocking buffer containing 8 µL 1:500 Alexa Fluor 647 and 4 µl 1:1000 DAPI. Primary antibody solution for *Aldh1l1* and *vimentin* staining: 2 ml blocking buffer containing 20 µl 1:100 anti-Aldh1l1 antibody (Abcam, AB56777) and 20 µl 1:100 anti-vimentin (Abcam, AB16700). Secondary antibody solution for *Aldh1l1* and *vimentin* staining: 4 ml blocking buffer containing 8 µl 1:500 Alexa Fluor 594, 8 µl 1:500 Alexa Fluor 647 and 4 µl 1:1000 DAPI.

Quantitative PCR on frog tadpole samples. Stress-related genes of *X. laevis* were selected from Xenbase[48], with a specific emphasis on genes that have been extensively researched and are supported by a substantial number of references.

Cryosection staining of cyborg mouse embryos. (1) Fixation: embryos were fixed with 4% PFA at 4 °C overnight, then soaked in 10% sucrose solution at 4 °C overnight; followed by 20% sucrose solution at 4 °C overnight. The soaked embryos were positioned in a cube chamber with Optimal Cutting Temperature compound (Tissue-Tek 4583) and frozen at −80 °C overnight for cryosection. (2) Staining: before staining, slides were placed in a wet box and incubated at 40 °C to remove residual Optimal Cutting Temperature compound. Then the slides were washed with 0.1% PBST for 15 min at room temperature and stained with 4 ml 0.1% PBST containing 4 µl DAPI overnight at 4 °C. Finally, slides were washed with 0.1% PBST 3 times and sealed.

Confocal imaging. Stained tissue slides were imaged with a Leica TCS SP8 confocal microscope using the Leica Application Suite X software platform 3.5.5 (https://www.leica-microsystems.com/products/microscope-software/p/leica-las-x-ls/downloads/). All the images were processed with Fiji (version 2.9.0).

Statistics and reproducibility. The experiments shown in Fig. 3a and Extended Data Fig. 1d were independently repeated more than 10 times with similar results. The experiments in Extended Data Figs. 5e and 8l–o was independently repeated more than 3 times with similar results.

Electrophysiology recording. All recordings were taken with a Blackrock CerePlex Direct recording system or an Intan RHD recording system. MATLAB and Python codes provided by Blackrock were used to load, view and convert raw data files into an accessible format for data analysis. For data acquisition, a Blackrock Microsystems CerePlex µ headstage or an Intan RHD recording headstage was connected to the flat flexible cable through a laboratory-made printed circuit board. The recording set-up was placed on an optic table and covered by a Faraday cage.

Animals reported in Fig. 4 were cultured in normal media until stage 27, after which they were placed cultured in an oxygen anaesthetic system to minimize movement during recording[56] (Extended Data Fig. 7a). The mesh electronics were connected to an amplification and data acquisition system via a flexible cable (Extended Data Fig. 7b).

For awake and behaving animal recording in Supplementary Fig. 8, cyborg tadpoles were cultured in normal media until stage 27, after which they were head-fixed using a previously reported agarose fixation method[57,58]. Specifically, a layer of agarose was cured on the agar scaffold of a head-fix set-up using an agar mould (Supplementary Fig. 8a, step 1). Then, the set-up was placed on top of the culture chamber (Supplementary Fig. 8a, step 2). Next, the tadpole was fixed using a small amount of low-melting-point agarose, with the scaffolds serving as anchor points (Supplementary Fig. 8a, step 3). The agarose was carefully trimmed to avoid covering the tadpole's mouth or tail, allowing it to breathe and move its tail once it recovered from the anaesthesia. After fixation, the lid was placed on top of the set-up to reduce media evaporation. Half of the media was changed every 12 h to increase the survival rate of the fixed tadpole.

The axolotl tadpoles reported in Fig. 6 were recorded every 12 h using the same set-up as the frog tadpoles (Extended Data Fig. 8b).

Data analysis

Analysis of fluorescence images. (1) Cell counting in Sox2 and Myt1 images: DAPI was used to identify the cell nuclei for accurate cell counting. Using Sox2 as an example, Sox2 image was first binarized to identify the region of neuron stem cells (Supplementary Fig. 4a, step 1). The binary Sox2 image was then overlaid with the DAPI image (Supplementary Fig. 4a, step 2), and DAPI-labelled cell nuclei in the Sox2 region were counted as the cell number of neuron stem cells (Supplementary Fig. 4a, step 3). (2) Fluorescence intensity of BrdU images: the DAPI image was binarized to identify the tissue region (Supplementary Fig. 4b, step 1). The binary DAPI image was then overlaid with the BrdU image (Supplementary Fig. 4b, step 2), and the fluorescence intensity of BrdU within the binary DAPI region was calculated (Supplementary Fig. 4b, step 3).

(3) Fluorescence intensity of *Aldh1l1* and *vimentin* images was analysed using Fiji (version 2.9.0).

Analysis of behaviour tests. Data from 1 to 3 DPF were not included, as tadpoles still could not swim. The behaviour videos were processed by MATLAB R2023b to analyse the trajectory of the tadpoles. (1) Colour preference test: the tadpole's distance to the white/black boundary was calculated and reported as 'tadpole to middle line' (Extended Data Fig. 6j). The percentage of time that the tadpole stayed in the white side of the tank was calculated and reported as the 'time ratio in white side', and the statistical results of all tested tadpoles are documented in Fig. 3o. (2) Visual avoidance: the tadpole's distance to the black dot was calculated and reported as 'tadpole to black dot' (Extended Data Fig. 6k). The percentage of successful escapes from the black dot was calculated and reported as the 'avoidance ratio', and the statistical results of all tested tadpoles are documented in Fig. 3p. (3) Edge preference: the tadpole's distance to the tank centre was calculated and reported as 'tadpole to centre' (Extended Data Fig. 6l). The percentage of time that the tadpole stayed in the tank edge (the area within 4 cm of the tank wall) was calculated and reported as the 'time ratio at the edge', and the statistical results of all tested tadpoles are documented in Fig. 3q.

Analysis of electrophysiological signals. The electrophysiological recording data were analysed offline with Python 3.7 and MATLAB R2023b. (1) Filtering of frog embryo and tadpole recordings: raw data were filtered using a low-pass filter in the <100 Hz frequency range for oscillation signals, a low-pass filter in the <300 Hz frequency range for calcium-wave-like signals, and a bandpass filter in the 300–3,000 Hz frequency range for spike-like signals. (2) Correlation analysis of frog embryo and tadpole recordings: for signals from stages 24 and 26 and local field potential signals in stage 40, 1 group of 4 synchronized peaks from each channel were extracted, and Pearson correlations were calculated between each pair of the synchronized peaks. Pearson correlations from all groups of synchronized peaks were then pooled for each stage. Apart from local field potentials, action potentials (spikes) were also extracted for stage 40 signals. Signal chunks from all channels were then extracted according to the time of spikes before the calculation of their pairwise Pearson correlations. Finally, the pooled Pearson correlations for each stage were compared. (3) Synchrony analysis of frog embryo and tadpole recording: for signals from stages 24 and 26 and local field potential signals in stage 40, the time differences between synchronized peaks in each pair of the channels were collected, generating 6 datasets for each stage. The standard deviation of each dataset indicated synchronization between two channels. The six standard deviations for each stage were then plotted and compared. (4) Spike sorting: all spike sorting was performed with a 300–3,000-Hz bandpass filter. Spike sorting of cyborg frog embryos and tadpoles was performed in MATLAB using WaveClus[59] and MountainSort[60]. Spike sorting of cyborg axolotl embryos and neonatal rats was performed using SpikeInterface[61]. (5) Correlation analysis of axolotl embryos recording: spikes from units were pooled with a bin size of 500 ms (refs. 62,63), and Pearson correlations were calculated based on the pooled spike counts using Elephant[39]. (6) Neural state analysis of axolotl embryos recording: changes in neural states during tail amputation were analysed using DataHigh[40].

Simulations

FEA. All FEA was performed using ABAQUS 2022/Standard. (1) Devices: PFPE–DMA and SU-8 ribbons were discretized by S4R elements. The material behaviour of the ribbons was captured using a linear elastic material model, with elastic modulus (E) and Poisson's ratio (ν) given by $E_{\mathrm{SU\text{-}8}} = 6$ GPa, $\nu_{\mathrm{SU\text{-}8}} = 0.4$ and $E_{\mathrm{PFPE}} = 500$ kPa, $\nu_{\mathrm{PFPE}} = 0.4$. The response of the ribbons was simulated by the *STATIC module. (2) Embryos: the tissue was discretized by the C3D4H element, with finer mesh size towards the neural plate. The material behaviour of the embryo tissue was characterized with shear modulus (μ) given by $\mu_{\mathrm{plate}} = 150$ Pa, $\mu_{\mathrm{ectoderm}} = 3$ kPa and $\mu_{\mathrm{inside\ tissue}} = 1.5$ Pa. The response of the tissue was captured by an incompressible neo-Hookean material model[64]. (3) Development simulation: a growth model[65] was used to mimic the embryo development. Volume-proportional damping was added using the option STABILIZE in the ABAQUS STATIC module (dissipated energy fraction equal to 5×10^{-4} and the maximum ratio of stabilization to strain energy equal to 0.05). The development was virtually driven by a thermal expansion of the embryo tissue, relating to the thermal strain $\varepsilon^{\mathrm{th}}$ through $\varepsilon^{\mathrm{th}} = \alpha(\theta - \theta^{\mathrm{I}})$, where α is the thermal expansion coefficient of the material, θ is the current temperature and θ^{I} is the initial temperature. In our simulations, $\alpha_{\mathrm{plate}} = 0.4\ \mathrm{K}^{-1}$, $\alpha_{\mathrm{inside\ tissue}} = 0.6\ \mathrm{K}^{-1}$ and $\alpha_{\mathrm{ectoderm}} = 1.0\ \mathrm{K}^{-1}$, the temperature θ was gradually increased until the neural plate formed a deep fold and encapsulated the device.

Reporting summary

Further information on research design is available in the Nature Portfolio Reporting Summary linked to this article.

Data availability

The gene sequences used in the qPCR assays were obtained from Xenbase: https://www.xenbase.org/xenbase/. All the other data supporting the findings of this study are available within the paper, Extended Data, Supplementary Information and source data.

Code availability

All the code is available on GitHub at https://github.com/LiuLab-Bioelectronics-Harvard/Cyborg_Embryo.

48. Karimi, K. et al. Xenbase: a genomic, epigenomic and transcriptomic model organism database. *Nucleic Acids Res.* **46**, D861–D868 (2018).
49. Aguilera-Castrejon, A. et al. Ex utero mouse embryogenesis from pre-gastrulation to late organogenesis. *Nature* **593**, 119–124 (2021).
50. Huang, Y., Wilkie, R. & Wilson, V. Methods for precisely localized transfer of cells or DNA into early postimplantation mouse embryos. *J. Vis. Exp.* **106**, e53295 (2015).
51. Lohmiller, J. J., Swing, S. P. & Hanson, M. M. in *The Laboratory Rat* 3rd edn (eds Suckow, M. A. et al.) 157–179 (Elsevier, 2020).
52. Vczian, A. S. & Zuber, M. E. A simple behavioral assay for testing visual function in *Xenopus laevis*. *J. Vis. Exp.* **88**, 51726 (2014).
53. Dong, W. et al. Visual avoidance in *Xenopus* tadpoles is correlated with the maturation of visual responses in the optic tectum. *J. Neurophysiol.* **101**, 803–815 (2009).
54. Pratt, K. G. & Khakhalin, A. S. Modeling human neurodevelopmental disorders in the *Xenopus* tadpole: from mechanisms to therapeutic targets. *Dis. Models Mech.* **6**, 1057–1065 (2013).
55. Klymkowsky, M. W. Whole-mount immunocytochemistry in *Xenopus*. *Cold Spring Harb. Protoc.* **2018**, pdb-prot097295 (2018).
56. Hamilton, P. W. & Henry, J. J. Prolonged in vivo imaging of *Xenopus laevis*. *Dev. Dyn.* **243**, 1011–1019 (2014).
57. Kamei, M. & Weinstein, B. M. Long-term time-lapse fluorescence imaging of developing zebrafish. *Zebrafish* **2**, 113–123 (2005).
58. Kamei, M., Isogai, S., Pan, W. & Weinstein, B. M. Imaging blood vessels in the zebrafish. *Methods Cell. Biol.* **100**, 27–54 (2010).
59. Chaure, F. J. et al. A novel and fully automatic spike-sorting implementation with variable number of features. *J. Neurophysiol.* **120**, 1859–1871 (2018).
60. Chung, J. E. et al. A fully automated approach to spike sorting. *Neuron* **95**, 1381–1394 (2017).
61. Buccino, A. P. et al. SpikeInterface, a unified framework for spike sorting. *eLife* **9**, e61834 (2020).
62. Bartolo, R., Saunders, R. C., Mitz, A. R. & Averbeck, B. B. Information-limiting correlations in large neural populations. *J. Neurosci.* **40**, 1668–1678 (2020).
63. Insel, N. & Barnes, C. A. Differential activation of fast-spiking and regular-firing neuron populations during movement and reward in the dorsal medial frontal cortex. *Cereb. Cortex* **25**, 2631–2647 (2015).
64. Ogden, R. W. *Non-linear Elastic Deformations* (Courier, 1997).
65. Amar, M. B. & Goriely, A. Growth and instability in elastic tissues. *J. Mech. Phys. Solids* **53**, 2284–2319 (2005).
66. Garaschuk, O., Hanse, E. & Konnerth, A. Developmental profile and synaptic origin of early network oscillations in the CA1 region of rat neonatal hippocampus. *J. Physiol.* **507**, 219–236 (1998).

Acknowledgements J.L. acknowledges the support from the Startup fund from the School of Engineering and Applied Sciences, Harvard University; NIH/NIMH 1RF1MH123948; Aramont Fund for Emerging Science Research; and the William F. Milton Fund. J.L. and N.L. acknowledge the support from NSF/EFRI 2422348. H. Sheng acknowledges the support from Aramont Fund for Emerging Science Research. J.L.W. and J.L. acknowledge the support from NIH/NICHD

1R01HD115272. X.W. acknowledges support from Packard Fellowship for Science and Engineering, Merkin Institute Fellowship, Stanley Center gift and NIH New Innovator Award. We thank D. J. Needleman for discussions.

Author contributions J.L. and H. Sheng conceived of the idea. R.L., H. Sheng, P.L.F., W.W. and A.J.L. fabricated and characterized electronics. H. Sheng performed implantation and behaviour tests. H. Sheng and Q.L. applied immunofluorescence. H. Sheng, Z.L. and J.B. did the qPCR. H. Sheng and R.L. performed electrical recordings. L.J., Z.W., H. Sheng, S.L. and N.L. did the mechanical simulation. R.A.J.-C. housed frogs. H. Sheng, H.Z., Z.L., Y.H., X.T., D.S., H.Z. and H. Shen analysed data. J.L.W. advised on designing tail amputation experiments. H. Sheng and E.H. prepared illustrations. H. Sheng, J.L., T.S.B. and X.W. wrote the draft of the paper. All authors revised the paper. J.L. supervised the study.

Competing interests H. Sheng, R.L., A.J.L. and J.L. are on a patent application filed by Harvard University related to this work. X.W. is a scientific co-founder and equity holder of Stellaromics and Convergence Bio. P.L.F. and J.L. are co-founders of Axoft Inc. The other authors declare no competing interests.

Additional information

Supplementary information The online version contains supplementary material available at https://doi.org/10.1038/s41586-025-09106-8.

Correspondence and requests for materials should be addressed to Jia Liu.

Peer review information *Nature* thanks Tal Dvir and the other, anonymous, reviewer(s) for their contribution to the peer review of this work.

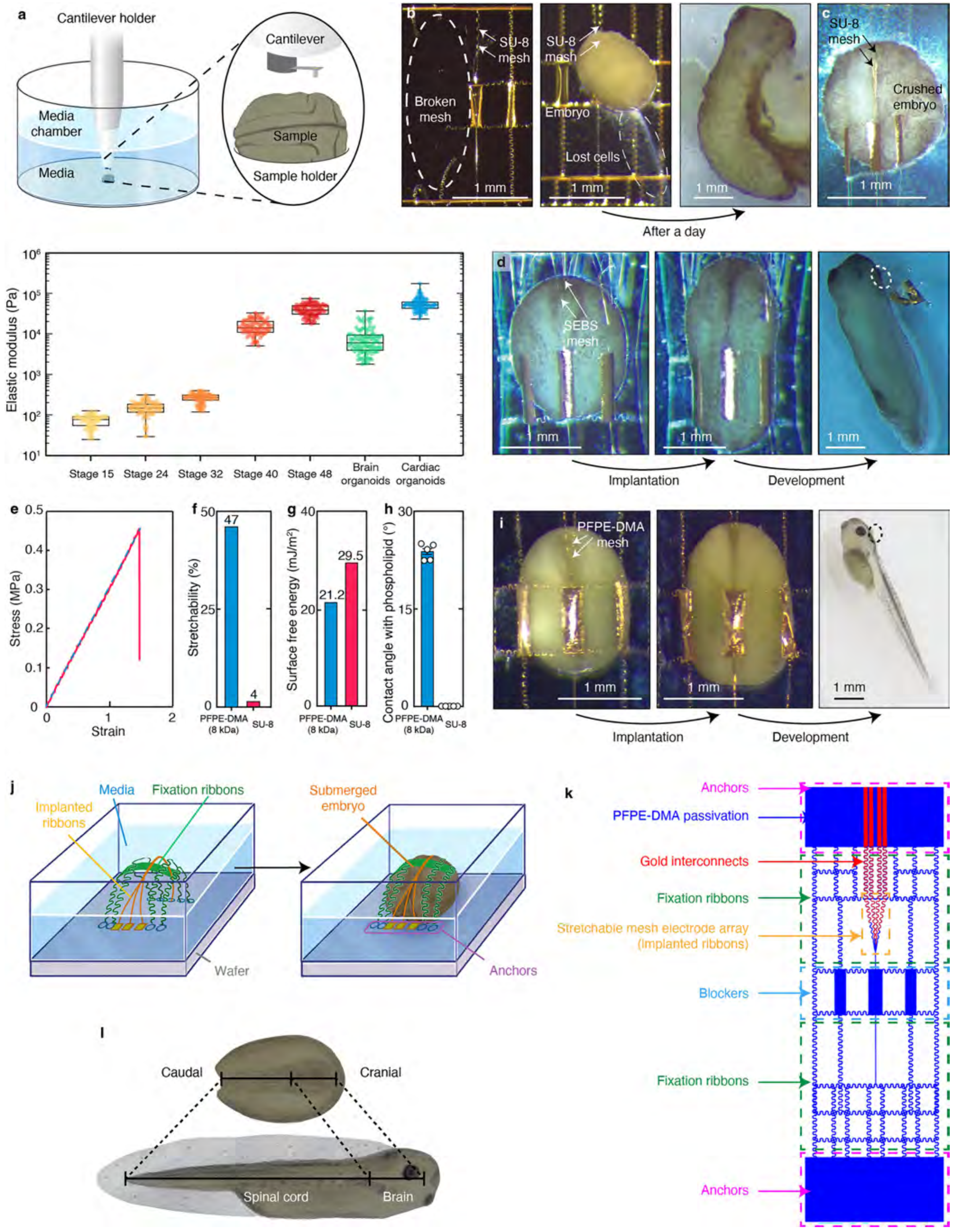

Extended Data Fig. 1 | See next page for caption.

Extended Data Fig. 1 | Test of implantation methods. a, (Top) schematics showing an atomic force microscopy (AFM) setup for tissue elastic modulus measurement. (Bottom) elastic modulus of stage 15, 24, 32, 40, 48 Xenopus embryos, brain organoids, and cardiac organoids. Box plots indicate minimum, lower quartile, median, upper quartile, and maximum. Each dot represents a contact measurement. **b**, Photographs showing broken SU-8 mesh post-implantation (left) and the embryo before (middle) and after (right) mesh implantation, depicting damage to the embryo. **c**, BF microscopic images showing an embryo crushed by SU-8 meshes. **d**, BF microscopic images showing an embryo successfully implanted with a SEBS mesh. The dashed line circle highlights the portion of the mesh which remains exterior to the tadpole brain. **e**, Stress-strain curve of PFPE-DMA film with 8 kDa molecular weight, the blue dashed line indicates a linear relationship. **f**, Stretchability of 8 kDa PFPE-DMA and SU-8 films. **g**, Surface free energy of 8 kDa PFPE-DMA film and SU-8 films. **h**, Contact angle of phospholipid (cell membrane analog) on 8 kDa PFPE-DMA film, and on SU-8 film. Bar plots indicate mean ± s.e.m., each dot represents a sample, $n = 5$. **i**, Photographic images showing an embryo successfully implanted with a PFPE-DMA mesh. The dashed line circle highlights the portion of the mesh which remains exterior to the tadpole brain. **j**, Schematics showing how anchors fix the stretchable mesh electronics to the substrate, keeping the neural plate properly positioned during neurulation for device internalization, and keeping the stretchable mesh electrode array attached to the neural plate. The device's initial dimensions and stretchability enable the stage 15 embryo to be slid under the device for implantation. **k**, The design of the stretchable mesh electronics showing the architecture of the stretchable mesh electrode array, stretchable serpentine interconnects, anchors, stretchable ribbons, and blockers. The blocker prevents the mesh electrodes from implanting into the caudal region of the neural plate. **l**, Schematics showing elongation of the neural tube during the embryo development of *Xenopus laevis*. The caudal region of the neural tube elongates to 3 times its initial length and forms the spinal cord while the cranial region elongates only 1.3 times its initial length and forms the brain.

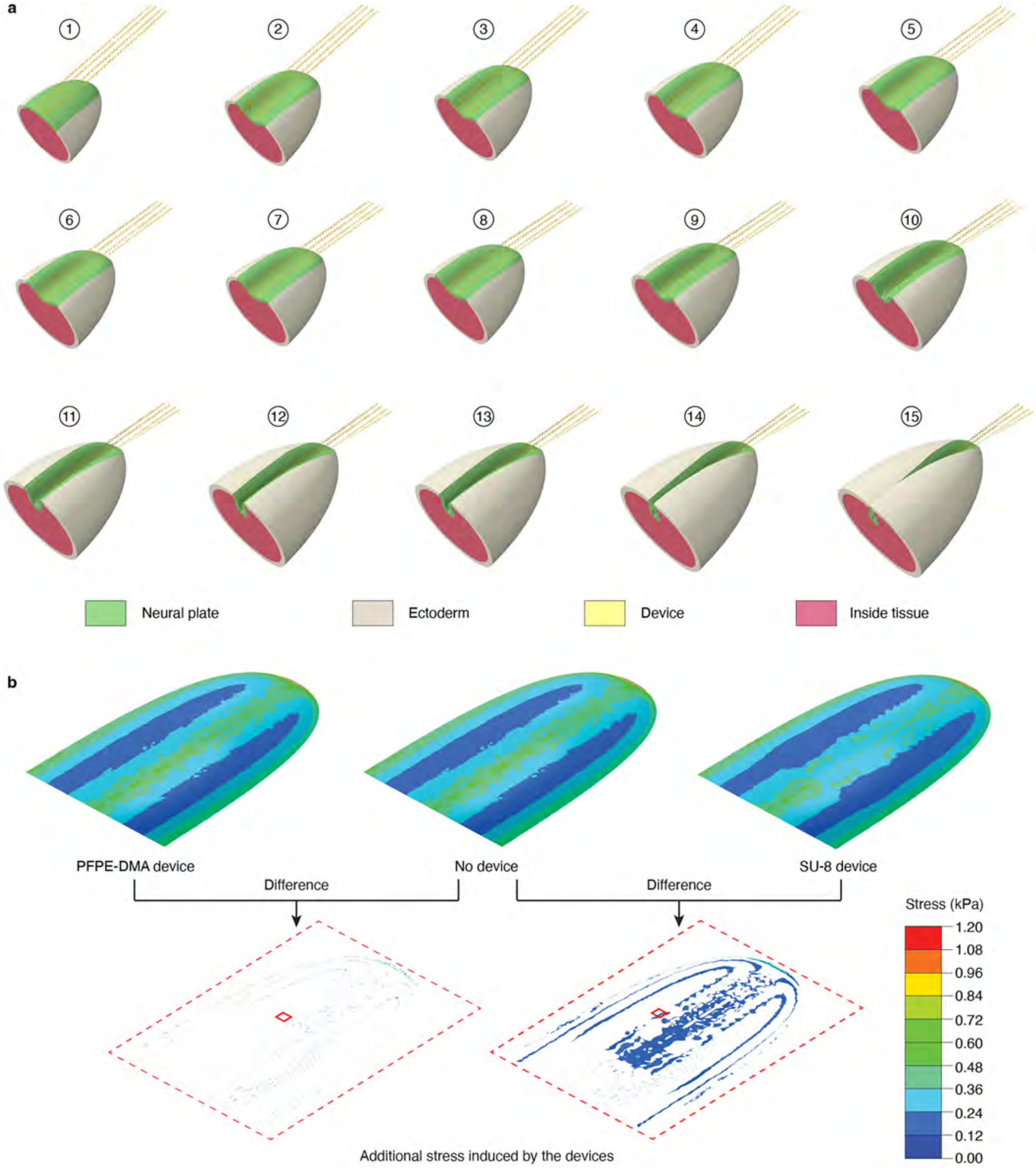

Extended Data Fig. 2 | Mechanical simulation of stretchable mesh for brain implantation via embryo development. a, Snapshots of mechanical simulation of mesh-neural plate interaction (Fig. 1j, k), labeled with sequenced numbers. **b**, Snapshots of mechanical simulation procedure showing the stress distribution in the neural plates with and without stretchable mesh implanted. An embryo simulation without mesh implantation was used as a reference to calculate the additional stresses introduced by PFPE-DMA and SU-8 meshes. The red boxes highlight regions where the maximum stress was shown in (Fig. 1k).

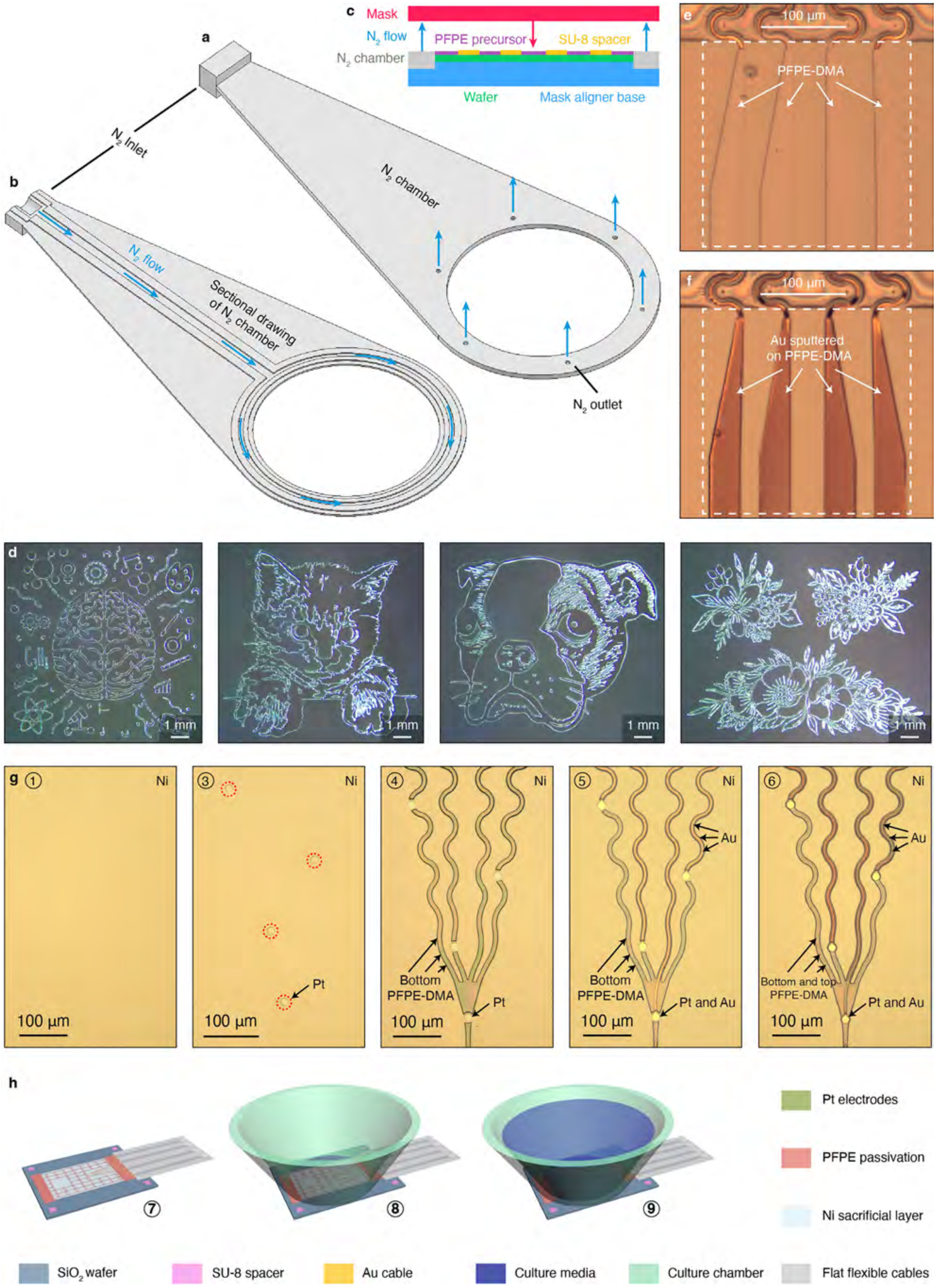

Extended Data Fig. 3 | See next page for caption.

Extended Data Fig. 3 | Fabrication of PFPE-DMA-encapsulated stretchable mesh electronics. a, b, Schematics showing the overlook (**a**) and section view (**b**) of the nitrogen chamber designed for use with the mask aligner in PFPE-DMA photopatterning. **c**, Schematic showing how the nitrogen chamber is used with mask aligner. **d**, Microscopic BF images showing representative high-resolution PFPE-DMA photolithography patterns made with the nitrogen chamber. **e, f**, Microscopic BF images showing the improved adhesion between Au interconnects and PFPE-DMA after inert gas plasma treatment. Dashed boxes highlight the sputtered regions on the PFPE-DMA layers. Without inert gas plasma treatment, Au interconnects peel off from the PFPE-DMA film after sputtering (**e**). With inert gas plasma treatment before sputtering, Au interconnects strongly bond to the PFPE-DMA film (**f**). **g**, Microscopic BF images showing the stretchable mesh electrode array region of PFPE-DMA device in fabrication steps corresponding to (Fig. 2c). Step 1 shows a homogeneous Ni layer. Step 2 is not included because the electrode array region does not have an SU-8 spacer. Step 3 shows Pt electrodes on the Ni layer. Electrodes are highlighted by red dashed circles. Steps 4-6 show sequential patterning of bottom PFPE-DMA, Au interconnects, and top PFPE-DMA layers. **h**, Schematics showing the post-fabrication steps of PFPE-DMA-encapsulated stretchable mesh electronics following (Fig. 2c). After fabrication, the device is soldered with a flexible flat cable (step 7) and bonded with a culture chamber (step 8). Then, the Ni layer is etched to release the device. Pt-black is electro-polymerized on electrodes to reduce electrode impedance. The device is washed with 0.1 × MMR and finally soaked in culture media (step 9).

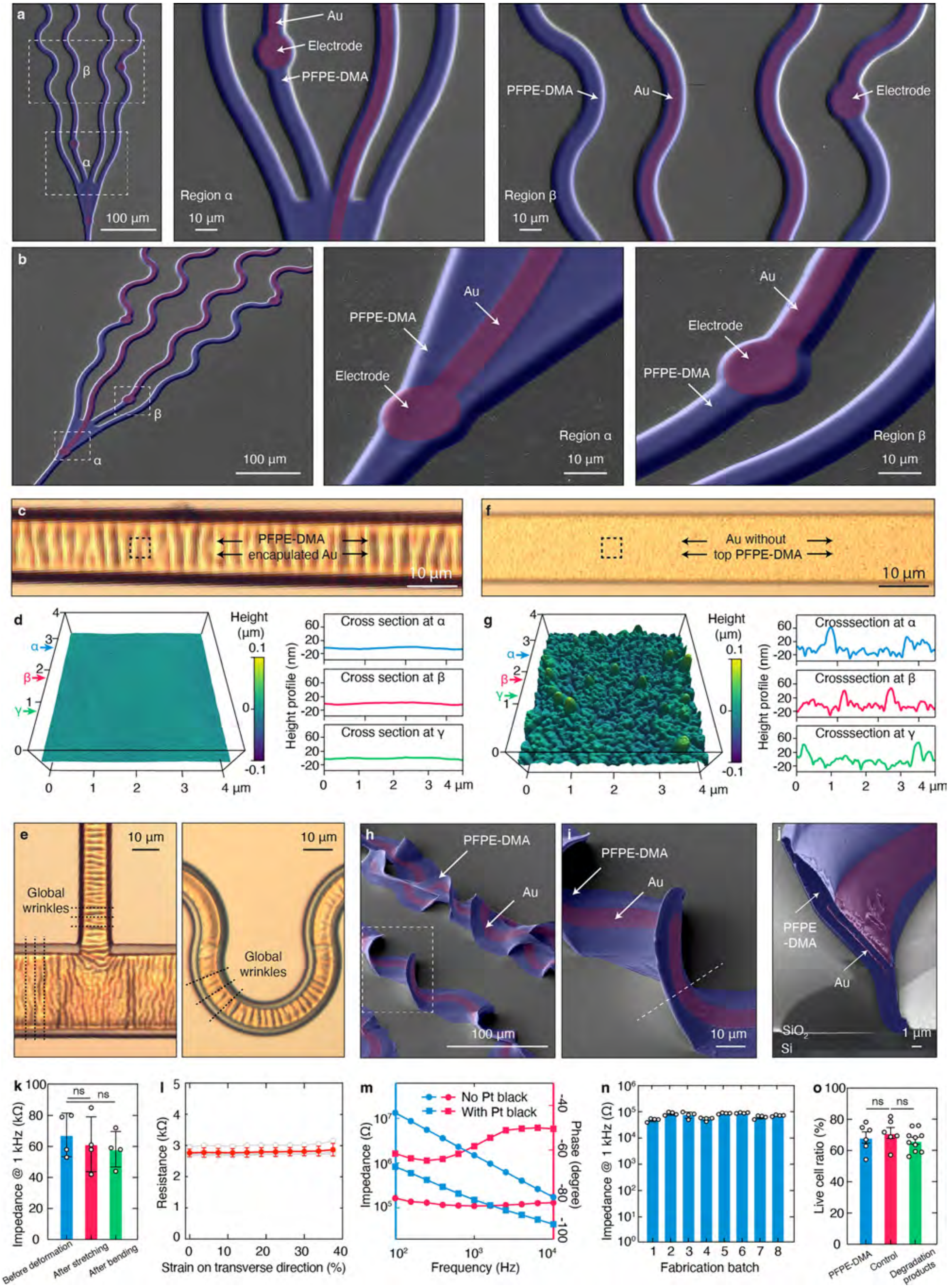

Extended Data Fig. 4 | See next page for caption.

Extended Data Fig. 4 | Characterization of PFPE-DMA-encapsulated stretchable mesh electronics. a, b, SEM images showing top views (**a**) and perspective views (**b**) of the stretchable mesh electrode array portion of the PFPE-DMA device. Each layer is pseudo-colored and labeled. **c**, BF image of a PFPE-DMA-encapsulated Au ribbon. **d**, (Left) atomic force microscopy (AFM) topography image of black dashed box-highlighted region in (**c**). (Right) height profiles of horizontal cross-sections highlighted in the left figure. **e**, BF images showing wrinkles of (left) straight and (right) serpentine PFPE-DMA-encapsulated interconnects. **f**, BF image of an Au interconnect without top PFPE-DMA passivation. **g**, (Left) AFM topography image of black dashed box-highlighted region in (**f**). (Right) height profiles of horizontal cross-sections highlighted in the left figure. **h**, SEM image showing perspective views of the PFPE-DMA stretchable mesh electronics after stretching and bending. **i**, SEM image of the dashed box-highlighted region in (**h**). **j**, SEM image showing cross-sections of PFPE-DMA-encapsulated Au interconnects, along the dashed line in (**i**). **h-j**, Each layer is pseudo-colored and labeled. **k**, Electrode impedance at 1 kHz in 37 °C PBS of PFPE-DMA mesh electronics before and after stretching and bending. Bar plots indicate mean ± s.e.m., each dot represents a single trial, two-tailed unpaired t-test, *n* = 4, ns, not significant. **l**, Resistance as a function of strain during the transverse stretch test of PFPE-DMA-encapsulated electronics. Red dots and line plots indicate mean ± s.d., and each gray dot and line plot represents one sample, *n* = 4. **m**, Electrochemical impedance spectroscopy of electrodes in stretchable mesh electronics with and without Pt-black coating. **n**, Electrode impedance at 1 kHz in 37 °C PBS of PFPE-DMA mesh electronics fabricated in different batches. Bar plots indicate mean ± s.e.m., each dot represents a sample, *n* = 4. **o**, Live cell ratio of wild-type rat cortical neurons after 10 days in vitro culture with PFPE-DMA mesh electronics, control, and with degradation products of PFPE-DMA. Bar plots indicate mean ± s.e.m., each dot represents a single trial, two-tailed unpaired t-test, *n* = 6, ns, not significant.

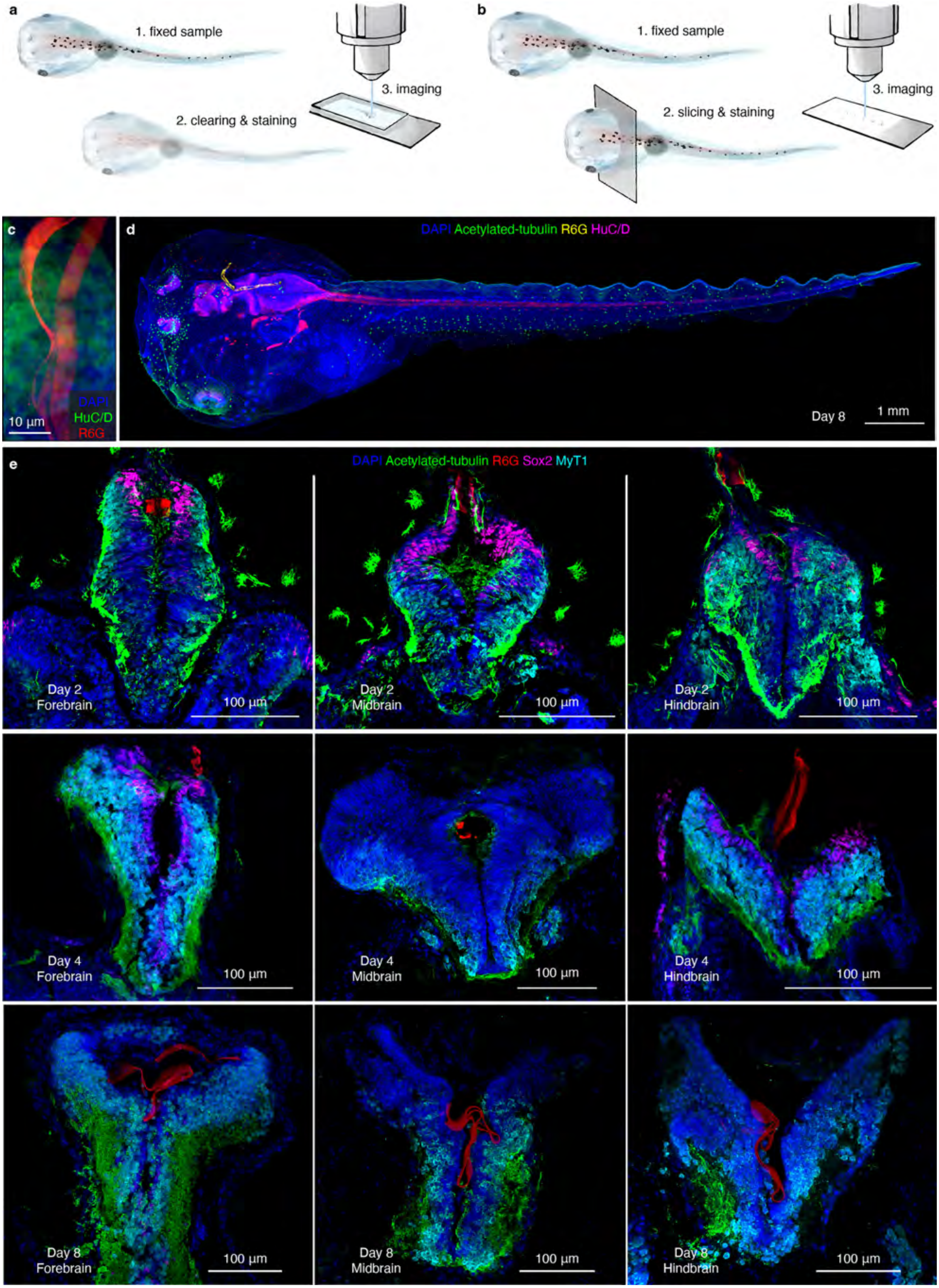

Extended Data Fig. 5 | See next page for caption.

Extended Data Fig. 5 | Staining methods and extended immunofluorescence images. a, b, Schematics showing the protocols for tissue clearing and whole-mount staining (**a**) and cryosection staining (**b**) to characterize brain tissue implanted with stretchable mesh electronics. **c**, Whole-mount-stained 3D reconstructed confocal fluorescence image of implanted mesh electronics showing that the mesh is embedded in the neural tissue. **d**, 3D reconstructed confocal fluorescence images of a whole-mount-stained cyborg tadpole whose device was implanted in the middle of neurulation. **e**, Confocal fluorescence images showing coronal sections of the fore-, mid-, and hindbrain of cyborg tadpoles fixed at 2-, 4- and 8-days post fertilization. In all images, DAPI labels cell nuclei, acetylated-tubulin labels basal bodies, R6G labels the device, and SRY-box transcription factor 2 (Sox2) labels neural stem cells. In fluorescence images of whole-mount staining samples, HuC/D labels neurons. In fluorescence images of cryosection staining samples, Myt1 labels neurons.

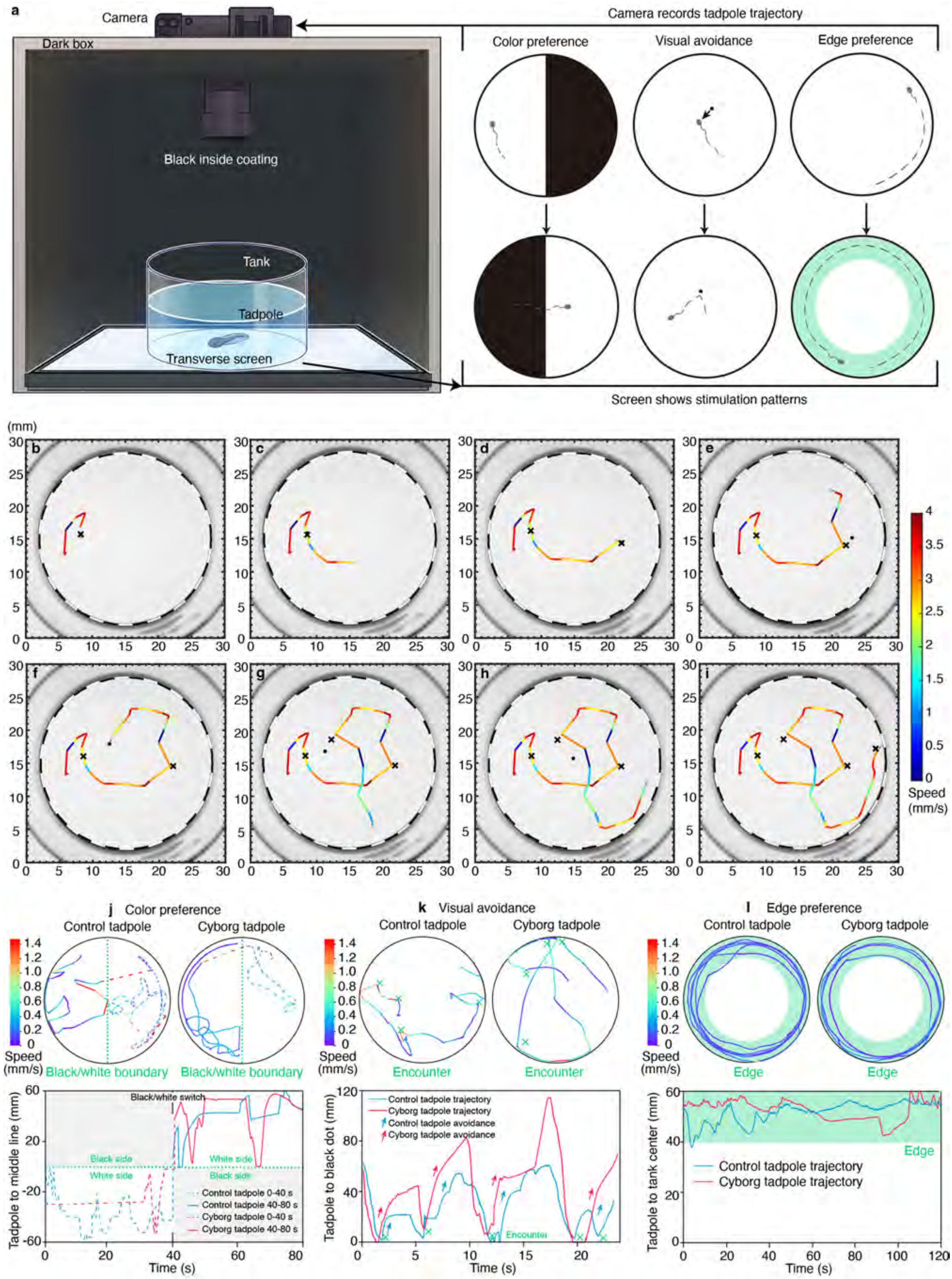

Extended Data Fig. 6 | See next page for caption.

Extended Data Fig. 6 | Experimental setup, trajectory analysis, and examples of behavior tests. a, Schematics showing the setup for behavioral testing. In each test, a tadpole is placed in a clear tank, sitting on an upward-facing screen. The screen is programmed to display the appropriate stimulation pattern for the color preference, visual avoidance, and edge preference tests. In the color preference test, the screen alternated between displaying half white and half black for 40 s each. In the visual avoidance test, a black dot is directly controllable via a computer mouse. The operator moved the dot toward the tadpole. If the tadpole responded, the operator would proceed to initiate the next encounter. If the tadpole did not respond, the operator would initiate a new encounter after five seconds. In the edge preference test, the entire screen is white. The setup is placed inside a dark box to minimize light contamination. The interior of the box is coated black to minimize reflections from the screen. Tadpoles are recorded using a video camera pointed down on the tank through a hole in the top of the box. **b-i**, Time-lapse snapshots of a visual avoidance video showing the trajectory process of a behaving tadpole. The colored lines connect the position of the tadpole in adjacent frames to form a trajectory. Crosses are labeled in frames where the tadpole met the black dot. **j-l**, Representative traces of behavior test data (top) and corresponding analyzed data (bottom). **j**, (Top) representative trajectories of tadpole movement in a color preference test. The green dotted lines indicate the boundary between the black and white areas. The right and left areas are white and black from 0–40 s, and switch colors from 40–80 s. Dashed and solid lines represent the trajectories of tadpole movement from 0–40 s and 40–80 s, respectively. (Bottom) distance of the tadpoles to the black and white boundary. Dashed and solid lines represent the trajectories of tadpole movement from 0–40 s and 40–80 s, respectively. Gray color highlights the black side. **k**, (Top) representative trajectories of tadpole movement in a visual avoidance test. Green crosses indicate the locations where the tadpole encountered the black dots. (Bottom) distance between the tadpole and the black dot during the test. **l**, (Top) representative trajectories of tadpoles in an edge preference test. The green ring indicates the outer quarter radius of the container defined as the edge in the experiment. (Bottom) distance between the tadpole and the container center during the test. The green color indicates the edge region. The statistical results of behavior tests, including examples in (**j-l**), were presented in Fig. 3o–q.

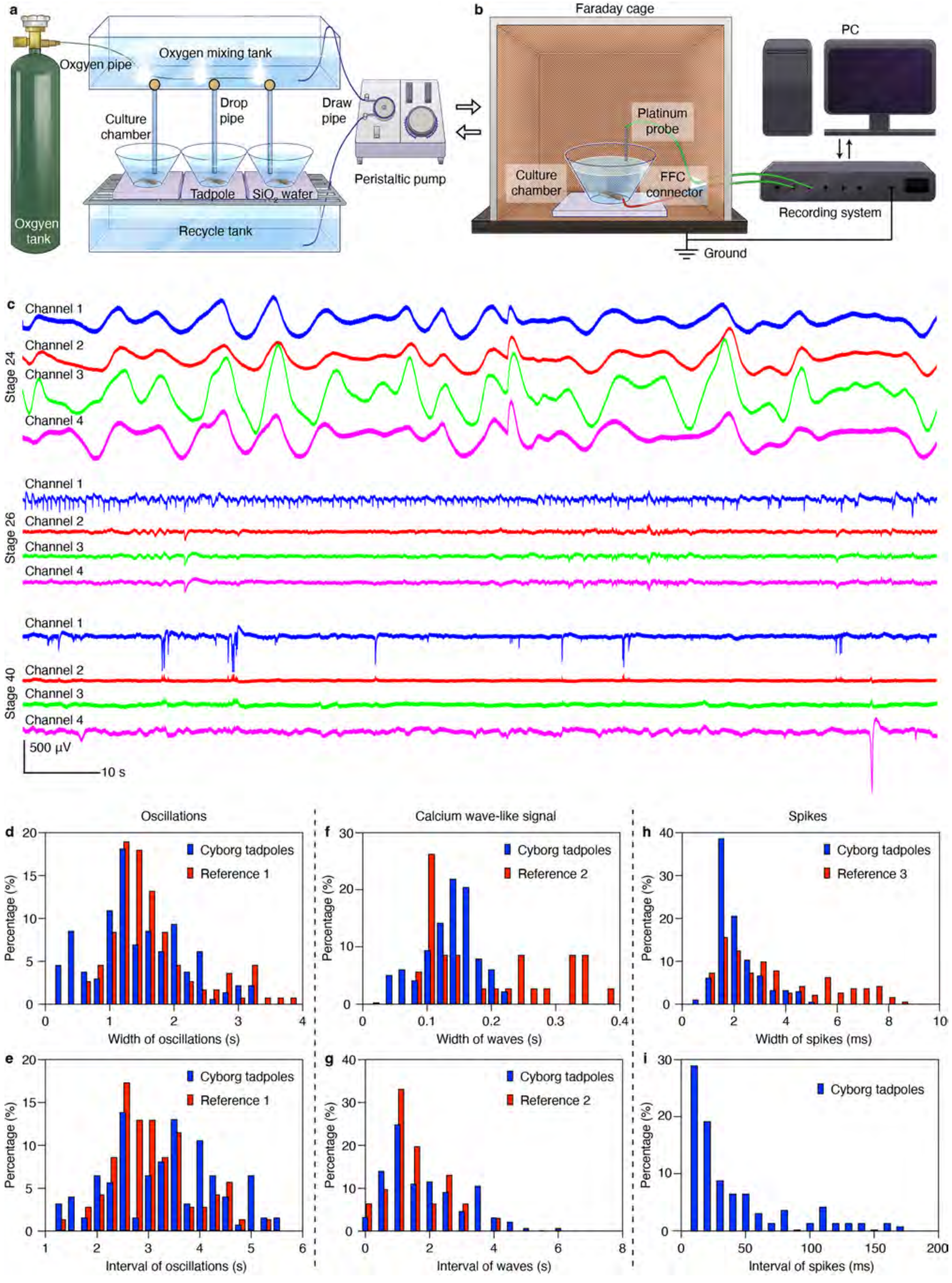

Extended Data Fig. 7 | See next page for caption.

Extended Data Fig. 7 | Experimental setup, raw data, and reference comparison of continuous electrophysiology in *Xenopus* embryonic brain development. a, Schematics showing the oxygen anesthetic system used to minimize tadpole movement during culture for recording. The system mixes the anesthetic media with fresh oxygen as previously reported[55] to minimize the effects of anesthesia on tadpole development. **b**, Schematics showing the recording setup for electrophysiological experiments. During recording, the culture chamber is placed in a Faraday cage on a grounded optic table. The input/output of the implanted mesh electronics is connected to a recording system using a flexible flat cable (FFC) connector. A Pt probe is placed in the culture media as ground. **c**, Raw data of continuous recordings shown in (Fig. 4). **d-i**, Reference comparison of continuous electrophysiology. Distribution plots showing comparisons of oscillation signal width (**d**) and interval (**e**); calcium-wave like signal width (**f**) and interval (**g**); spike width (**h**) and interval (**i**). Reference data is as follows: reference 1[66], reference 2[34], and reference 3[35]. Reference 3 did not include the corresponding dataset for spike intervals, so it is not included in (**i**). The results in (**d-i**) are determined from signals collected from three cyborg tadpoles.

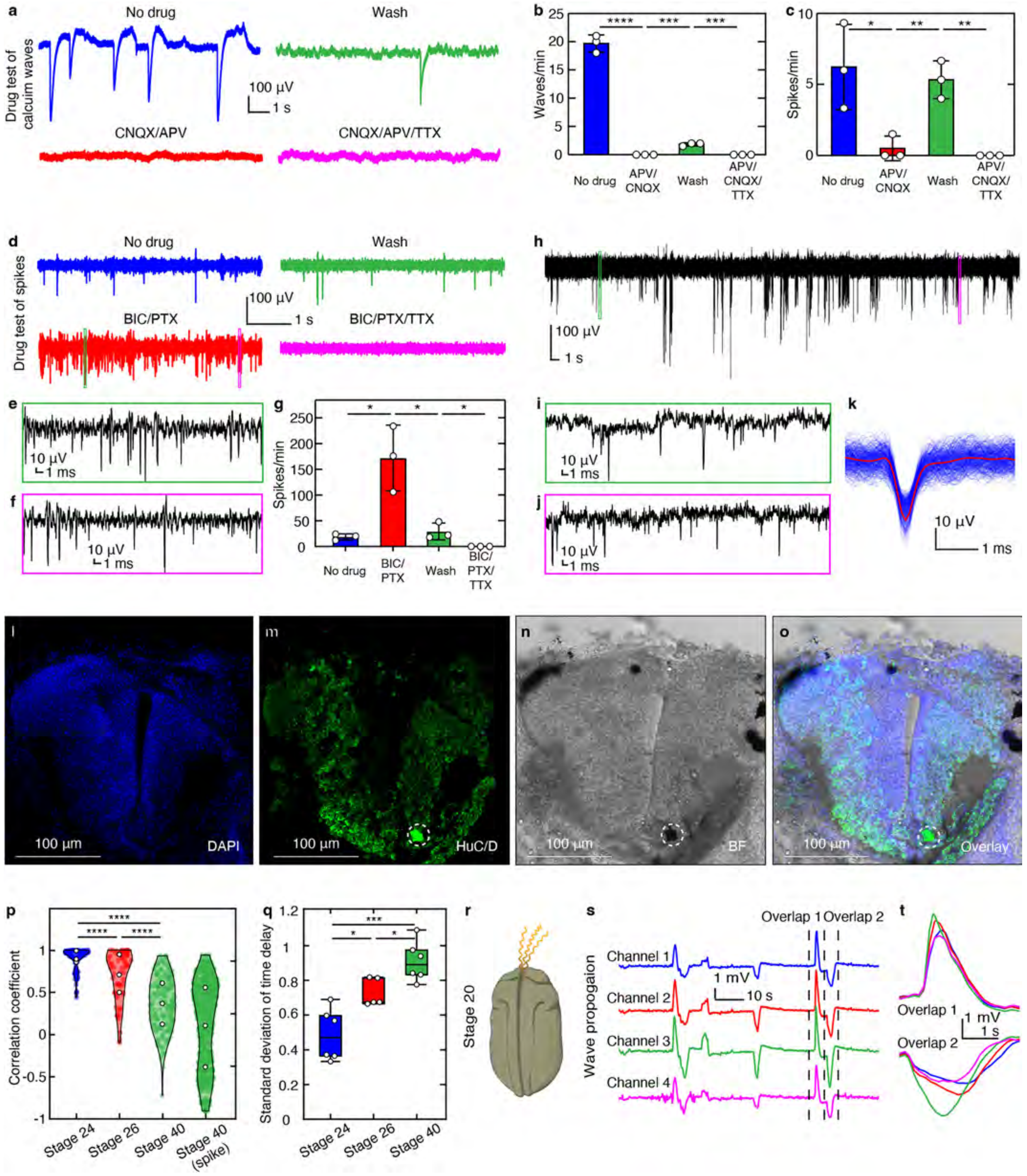

Extended Data Fig. 8 | See next page for caption.

Extended Data Fig. 8 | Analysis of continuous electrophysiology in *Xenopus* embryonic brain development. a-g, Pharmacological tests. **a**, Dynamics of calcium wave-like signals during the pharmacological test. Representative voltage traces from the cyborg tadpole under serial pharmacological test conditions of no drug, cyanquixaline (CNQX)/[2 R]-amino-5-phosphonopentanoate (APV), wash of CNQX/APV, and CNQX/APV/ tetrodotoxin (TTX). **b**, The change of wave number per minute during the pharmacological test. Bar plots indicate mean ± s.d., each dot represents a recording trial, two-tailed unpaired t-test, $n = 3$, No drug vs APV/CNQX, ****, $p < 0.0001$; APV/CNQX vs. Wash, ***, $p = 0.0004$; Wash vs. APV/CNQX/TTX, ***, $p = 0.0004$. **c-g**, Dynamics of spike-like signals during the pharmacological test. **c**, Statistical summary of the firing rate changes under different conditions. The tadpole was treated with APV/CNQX, washed, then CNQX/APV/ TTX in series. Bar plots indicate mean ± s.d., each dot represents a recording trial, two-tailed unpaired t-test, $n = 3$, No drug vs. APV/CNQX, *, $p = 0.0343$; APV/CNQX vs. Wash, **, $p = 0.0064$; Wash vs. APV/CNQX/TTX, **, $p = 0.0024$. **d**, Representative voltage traces from the cyborg tadpole under serial pharmacological test conditions of no drug, bicuculline (BIC)/picrotoxin (PTX), washed, followed by BIC/PTX/TTX. **e, f**, Zoomed-in views of the signal highlighted by the green (**e**) and magenta (**f**) boxes in (**d**). **g**, Statistical summary of the firing rate changes under different conditions. The tadpole was treated with BIC/PTX, washed, then BIC/PTX/TTX in series. Bar plots indicate mean ± s.d., each dot represents a recording trial, two-tailed unpaired t-test, $n = 3$, No drug vs. BIC/PTX, *, $p = 0.0146$; BIC/PTX vs. Wash, *, $p = 0.0202$; Wash vs. BIC/PTX/TTX, *, $p = 0.0356$. **h-o**, Correlation of single-unit action potential signals with the corresponding electrode position. **h**, Representative voltage traces from a cyborg tadpole showing single-unit action potentials. **i, j**, Zoomed-in views of the signal highlighted by green (**i**) and magenta (**j**) boxes in (**h**). **k**, Mean spike superimposed on all spikes from the same unit, sorted by spike sorting of data in (**h**). **l-o**, Confocal fluorescence images of the cyborg tadpole brain slice showing DAPI (**l**), HuC/D (**m**), BF (**n**) and overlaid (**o**) channels. The white dashed circles highlight the position of the electrode that recorded the voltage trace in (**h**). **p**, Correlation coefficient between channels of stages 24, 26, stage 40 local field potential and stage 40 spike signals. Positive correlation corresponds to a coefficient of 1, negative to -1, and no correlation to 0. White dots represent the lower quartile, median, upper quartile from bottom to top. Each translucent dot represents a sample, two-tailed unpaired t-test, ****, $p < 0.0001$. **q**, Standard deviation of time delay between channels of stages 24, 26, and 40 local field potential signals. Lower standard deviations indicate greater synchronization between channels. Upper and lower whiskers of the box plots represent maximum and minimum. Top, middle, and bottom lines of the box plots represent upper quartile, median and lower quartile. Each white dot represents a sample, two-tailed unpaired t-test, $n \geq 5$, Stage 24 vs. Stage 26, *, $p = 0.0102$; Stage 26 vs. Stage 40, *, $p = 0.0162$; Stage 24 vs. Stage 40, ***, $p = 0.0003$. **r-t**, Propagating wave signals in stage 20 embryonic brain. **r**, Schematic of the cyborg tadpole at developmental stage 20. **s**, Representative voltage traces from four channels in the cyborg tadpole at stage 20. **t**, Zoomed-in views of the signals highlighted by dashed lines in (**s**).

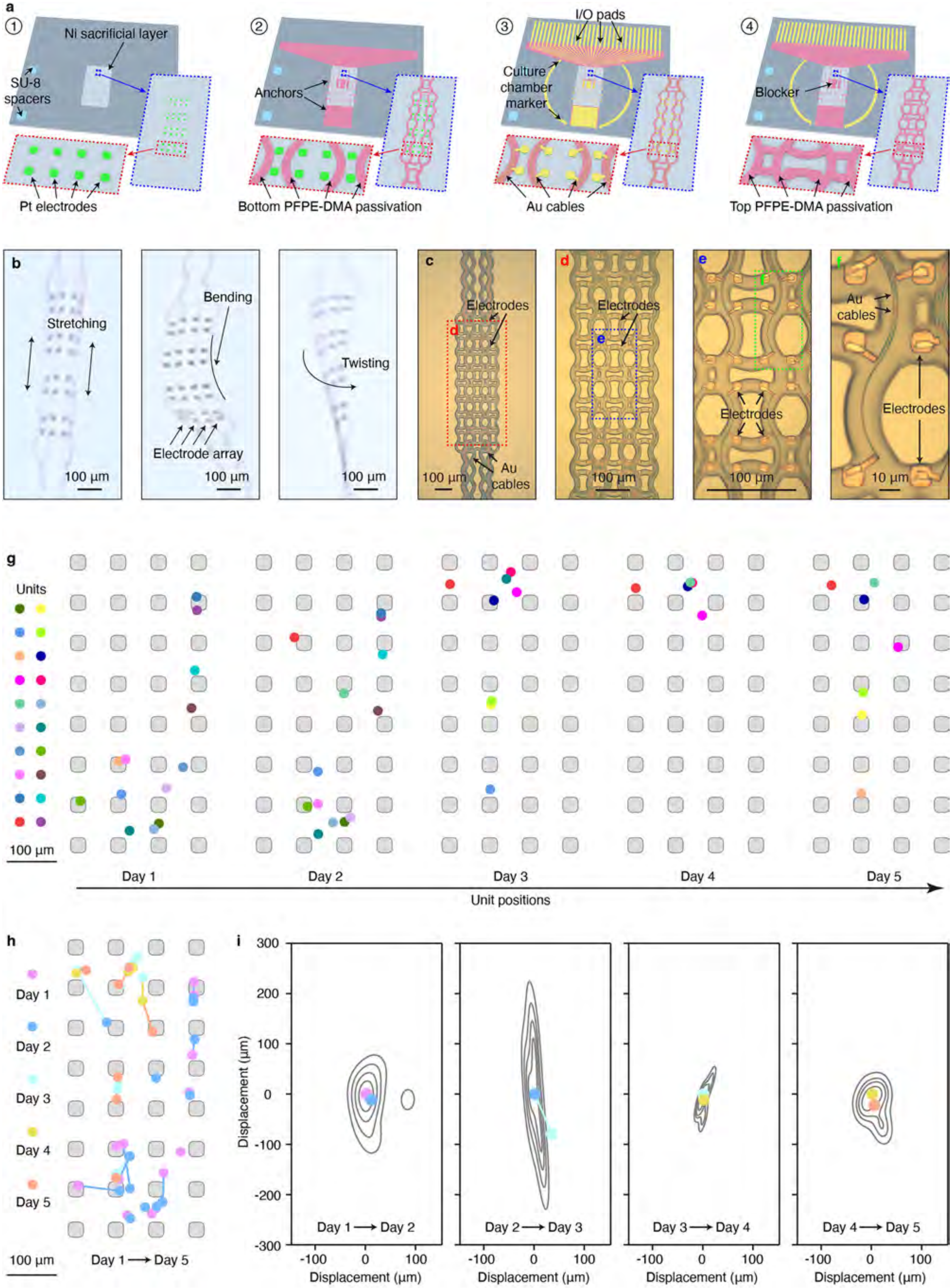

Extended Data Fig. 9 | See next page for caption.

Extended Data Fig. 9 | Soft and stretchable high-density mesh electrode array for tracking neural activities. a, Schematics showing the electron-beam (e-beam) lithographic fabrication of PFPE-DMA-encapsulated stretchable mesh electronics with a 32-channel high-density electrode array. First, a Ni layer is deposited on a blank silicon oxide wafer as a sacrificial layer. A SU-8 layer is patterned as a spacer, Pt electrodes are photolithographically patterned (step 1). Then, the bottom PFPE-DMA (step 2), Au interconnects (step 3), and top PFPE-DMA layer (step 4) are lithographically patterned. Au layer is patterned by e-beam lithography. PFPE-DMA layers are patterned by photolithography. Zoomed-in images show the details of the electrode arrays (highlighted in blue dashed boxes) and individual electrodes (highlighted in red dashed boxes). **b**, Photographic images showing the free-floating 32-channel high-density electrode array during stretching, bending, and twisting. **c**, BF microscopic image showing a representative 128-channel electrode array. **d**, Zoomed-in view of the red dashed box-highlighted region in (**c**) showing the high-density electrodes and interconnects. **e**, Zoomed-in view of the blue dashed box-highlighted region in (**d**) showing the stretchable design. **f**, Zoomed-in view of the green dashed box-highlighted region in (**e**) showing the individual electrodes and interconnects. **g**, Single-unit waveform centroids (*n* = 20 neurons) from the continuous 5-day recording of the cyborg axolotl embryo in (Fig. 5). Centroid computed using spatial average across electrode positions weighted by the square of the mean waveform amplitude at each electrode. Grey patterns indicate the positions and sizes of the mesh electrodes. **h**, Single-unit waveform centroid displacement throughout the 5-day recording in (Fig. 5). Centroids from the same day are labeled with the same color. Centroids for the same units across different days are connected by lines. Grey patterns indicate the positions and sizes of the mesh electrodes. **i**, Average displacement of single-unit centroids across different days of the 5-day recording in (Fig. 5). Grey contours indicate quintile boundaries of the distribution of centroid position displacement.

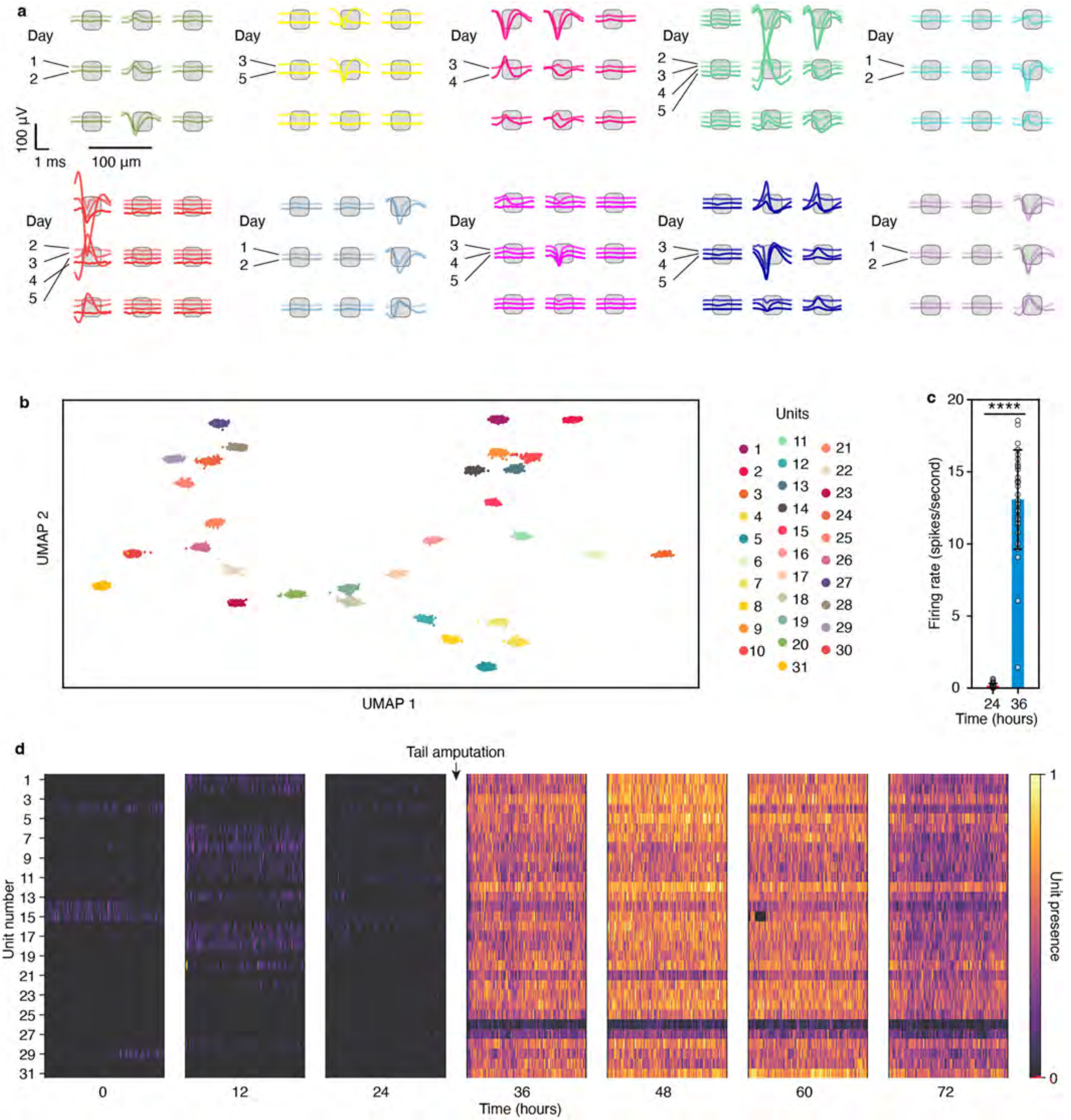

Extended Data Fig. 10 | Single-unit action potential in axolotl embryonic brain development. **a**, Representative average single-unit waveforms recorded from the same neurons overlaid with extremum electrodes over the 5-day recording period in (Fig. 5). **b**, UMAP visualization of units sorted from the continuous recording of the tail-amputated cyborg axolotl embryo, as shown in (Fig. 6). **c**, Firing rates of units recorded immediately before and after tail amputation of cyborg axolotl embryo, as shown in (Fig. 6). Bar plots indicate mean ± s.d., with individual dots representing firing rate of individual units, two-tailed unpaired t-test, $n = 30$, ****, $p < 0.0001$. **d**, Normalized presence of units sorted from continuous recording of the tail-amputated axolotl embryo, as shown in (Fig. 6).

nature portfolio

Corresponding author(s): Jia Liu
Last updated by author(s): Mar 27, 2025

Reporting Summary

Nature Portfolio wishes to improve the reproducibility of the work that we publish. This form provides structure for consistency and transparency in reporting. For further information on Nature Portfolio policies, see our Editorial Policies and the Editorial Policy Checklist.

Statistics

For all statistical analyses, confirm that the following items are present in the figure legend, table legend, main text, or Methods section.

n/a	Confirmed	
☐	☒	The exact sample size (*n*) for each experimental group/condition, given as a discrete number and unit of measurement
☐	☒	A statement on whether measurements were taken from distinct samples or whether the same sample was measured repeatedly
☐	☒	The statistical test(s) used AND whether they are one- or two-sided *Only common tests should be described solely by name; describe more complex techniques in the Methods section.*
☒	☐	A description of all covariates tested
☒	☐	A description of any assumptions or corrections, such as tests of normality and adjustment for multiple comparisons
☐	☒	A full description of the statistical parameters including central tendency (e.g. means) or other basic estimates (e.g. regression coefficient) AND variation (e.g. standard deviation) or associated estimates of uncertainty (e.g. confidence intervals)
☐	☒	For null hypothesis testing, the test statistic (e.g. *F*, *t*, *r*) with confidence intervals, effect sizes, degrees of freedom and *P* value noted *Give P values as exact values whenever suitable.*
☒	☐	For Bayesian analysis, information on the choice of priors and Markov chain Monte Carlo settings
☒	☐	For hierarchical and complex designs, identification of the appropriate level for tests and full reporting of outcomes
☐	☒	Estimates of effect sizes (e.g. Cohen's *d*, Pearson's *r*), indicating how they were calculated

Our web collection on statistics for biologists contains articles on many of the points above.

Software and code

Policy information about availability of computer code

Data collection	All recordings were taken with a Blackrock CerePlex Direct recording system or an Intan RHD recording system. MATLAB and Python codes provided by Blackrock were used to load, view, and convert raw data files into an accessible format for data analysis. Stained tissue slides were imaged with a Leica TCS SP8 confocal microscope using the Leica Application Suite X software platform 3.5.5 (https://www.leica-microsystems.com/products/microscope-software/p/leica-las-x-ls/downloads/). All the images were processed with Fiji (version 2.9.0).
Data analysis	Custom-designed codes were built with Python 3.7 and MATLAB R2023b for behavior video analysis (Trajectory_colorpreference, Trajectory_edgepreference, Trajectory_visualavoidance), cell counting of cyrosections (Cellcounting_cyrosection), correlation and synchronization analyses of continuous electrophysiology (Correlation_sycronization_analyses), heat map and time delay plot of continuous electrophysiology (Heatmap_timedelay_electrophysiology), comprehensive analysis of electrophysiology (Comprehensive electrophysiology analysis), tail amputation analyses (Tail_amputation_analyses). The detailed implementation can be found in GitHub repository at https://github.com/LiuLab-Bioelectronics-Harvard/Cyborg_Embryo.

For manuscripts utilizing custom algorithms or software that are central to the research but not yet described in published literature, software must be made available to editors and reviewers. We strongly encourage code deposition in a community repository (e.g. GitHub). See the Nature Portfolio guidelines for submitting code & software for further information.

Data

Policy information about availability of data

All manuscripts must include a data availability statement. This statement should provide the following information, where applicable:

- Accession codes, unique identifiers, or web links for publicly available datasets
- A description of any restrictions on data availability
- For clinical datasets or third party data, please ensure that the statement adheres to our policy

Gene sequences used in quantitative polymerase chain reaction assays are obtained from Xenbase: https://www.xenbase.org/xenbase/. All the other data supporting the findings of this study are available within the paper, Extended Data, Supplementary information and source data.

Human research participants

Policy information about studies involving human research participants and Sex and Gender in Research.

Reporting on sex and gender	NA
Population characteristics	NA
Recruitment	NA
Ethics oversight	NA

Note that full information on the approval of the study protocol must also be provided in the manuscript.

Field-specific reporting

Please select the one below that is the best fit for your research. If you are not sure, read the appropriate sections before making your selection.

☒ Life sciences ☐ Behavioural & social sciences ☐ Ecological, evolutionary & environmental sciences

For a reference copy of the document with all sections, see nature.com/documents/nr-reporting-summary-flat.pdf

Life sciences study design

All studies must disclose on these points even when the disclosure is negative.

Sample size	No statistical method was used to predetermine sample size. Sample size for each experiment were selected based on commonly accepted standards in the filed, and to ensure reproducibility across multiple independent replicates.
Data exclusions	For eletrophysiological analysis, we used standard algorithms, Wave_clus or Mountainsort, to detect the spikes which passed the threshold.
Replication	All the results were collected from multiple samples. Experiments were independently repeated at least 3 times with similar results. Details were included in of “Statistics and Reproducibility” in Method. All attempts at replication were successful.
Randomization	The randomization is not applicable the experiments because the experimental designs did not involve treatment allocation across different experimental groups. All samples were subjected to identical conditions, and comparisons were made between clearly defined biological or experimental categories (test group vs control group).
Blinding	Blinding was not used. Measurements and data reported were quantitative and did not require subjective judgement from the investigators.

Reporting for specific materials, systems and methods

We require information from authors about some types of materials, experimental systems and methods used in many studies. Here, indicate whether each material, system or method listed is relevant to your study. If you are not sure if a list item applies to your research, read the appropriate section before selecting a response.

Materials & experimental systems

n/a	Involved in the study
☐	☒ Antibodies
☒	☐ Eukaryotic cell lines
☒	☐ Palaeontology and archaeology
☐	☒ Animals and other organisms
☒	☐ Clinical data
☒	☐ Dual use research of concern

Methods

n/a	Involved in the study
☒	☐ ChIP-seq
☒	☐ Flow cytometry
☒	☐ MRI-based neuroimaging

Antibodies

Antibodies used	Recombinant Anti-HuD + HuC antibody (Abcam, AB184267); Anti-Acetylated Tubulin antibody, Mouse monoclonal (Sigma-Aldrich, T7451); BrdU Monoclonal Antibody (MoBU-1) (Invitrogen, B35128); Anti-SOX2 Monoclonal (clone name: Btjce) (Invitrogen, 14-9811-82); Anti-Myt1/MTF1 antibody (Abcam, AB251682); Anti-vimentin antibody (SP20) (Abcam, AB16700); Ms mAb to ALDH1L1 (3E9) (Abcam, AB56777); Anti-NeuN Antibody [1B7] - Neuronal Marker (Abcam, AB104224); Goat anti-Rat IgG (H+L) Cross-Adsorbed Secondary Antibody, Alexa Fluor™ 488 (Invitrogen, A-11006); Goat anti-Rabbit IgG (H+L) Cross-Adsorbed Secondary Antibody, Alexa Fluor™ 594 (Invitrogen, A-11012); IgG (H+L) Highly Cross-Adsorbed Donkey anti-Mouse, Alexa Fluor™ Plus 647 (Invitrogen, A-32787); Goat anti-Rabbit IgG (H+L) Highly Cross-Adsorbed Secondary Antibody, Alexa Fluor™ Plus 488 (Invitrogen, A-32731); Alexa Fluor™ 647 Phalloidin (Thermo Fisher SCIENTIFIC, A22287)
Validation	All primary antibodies used in this study are validated for the species and applications by the manufacturers. They have all been used in previous publications by us and others. Primary antibodies: Anti-HuD + HuC antibody (Abcam, AB184267): Abcam provides several references for validation : https://www.abcam.com/en-us/products/primary-antibodies/hud-huc-antibody-epr19098-ab184267 Anti-Acetylated Tubulin antibody, Mouse monoclonal (Sigma-Aldrich, T7451): Sigma-Aldrich provides several references for validation: https://www.sigmaaldrich.com/US/en/product/sigma/t7451?srsltid=AfmBOoqKGagPCFhoTW_C693OXLj8sblXtb58UDBDQEYMAJSUnAoBhJdi BrdU Monoclonal Antibody (MoBU-1) (Invitrogen, B35128): ThermoFisher SCIENTIFIC provides several references for validation: https://www.thermofisher.com/antibody/product/BrdU-Antibody-clone-MoBU-1-Monoclonal/B35128 Anti-SOX2 Monoclonal (clone name: Btjce) (Invitrogen, 14-9811-82): ThermoFisher SCIENTIFIC provides several references for validation: https://www.thermofisher.com/antibody/product/SOX2-Antibody-clone-Btjce-Monoclonal/14-9811-82 Anti-Myt1/MTF1 antibody (Abcam, AB251682): We tested it at dilutions recommended by the manufacturers to ensure that labeled cell structures exhibited strong fluorescence relative to background staining. Anti-vimentin antibody (SP20) (Abcam, AB16700): Abcam provides several references for validation : https://www.abcam.com/en-us/products/primary-antibodies/vimentin-antibody-sp20-ab16700?srsltid=AfmBOopNJgBxkO2iNFfVfQsupIu9iNCu43bV0OJeSftxbs6cTiay_IE0 Ms mAb to ALDH1L1 (3E9) (Abcam, AB56777): Abcam provides several references for validation : https://www.abcam.com/en-us/products/primary-antibodies/aldh1l1-antibody-3e9-ab56777?srsltid=AfmBOooH3sQfSKgJlRmNd9E56HaPaL3snyBGFm2h_h_b6Er5alPMJd-j Anti-NeuN Antibody [1B7] - Neuronal Marker (Abcam, AB104224): Abcam provides several references for validation : https://www.abcam.com/en-us/products/primary-antibodies/neun-antibody-1b7-neuronal-marker-ab104224?srsltid=AfmBOooGcNqFKxjzeaVfMW2HSpjrzVFOZxZYha2VhQUKf8tAGdGqz7se

Animals and other research organisms

Policy information about studies involving animals; ARRIVE guidelines recommended for reporting animal research, and Sex and Gender in Research

Laboratory animals	Wild-type Xenopus laevis emrbyos (fertilization to stag 65); wild-type axolotl emrbyos (fertilization to stage 38); CD female rats (<8 months old) ; C57BL/6 female mice (<6 months old)
Wild animals	None.
Reporting on sex	Sex of Xenopus laevis and axolotl embryos was not considered in experimental design. Sex of rodent are reported properly.
Field-collected samples	None.
Ethics oversight	Experimental procedures were approved by the Institutional Animal Care and Use Committee (IACUC) of Harvard under animal protocol # 19-01-344-1 and # 19-01-348-1.

Note that full information on the approval of the study protocol must also be provided in the manuscript.